Comparisons of Instantaneous TRMM Ground Validation and Satellite Rain-Rate Estimates at Different Spatial Scales

DAVID B. WOLFF AND BRAD L. FISHER

Science Systems and Applications, Inc., Lanham, and NASA Goddard Space Flight Center, Greenbelt, Maryland

(Manuscript received 14 September 2007, in final form 3 January 2008)

ABSTRACT

This study provides a comprehensive intercomparison of instantaneous rain rates observed by the two rain sensors aboard the Tropical Rainfall Measuring Mission (TRMM) satellite with ground data from two regional sites established for long-term ground validation: Kwajalein Atoll and Melbourne, Florida. The satellite rain algorithms utilize remote observations of precipitation collected by the TRMM Microwave Imager (TMI) and the Precipitation Radar (PR) aboard the TRMM satellite. Three standard level II rain products are generated from operational applications of the TMI, PR, and combined (COM) rain algorithms using rain information collected from the TMI and the PR along the orbital track of the TRMM satellite. In the first part of the study, $0.5° \times 0.5°$ instantaneous rain rates obtained from the TRMM 3G68 product were analyzed and compared to instantaneous Ground Validation (GV) program rain rates gridded at a scale of $0.5° \times 0.5°$. In the second part of the study, TMI, PR, COM, and GV rain rates were spatiotemporally matched and averaged at the scale of the TMI footprint ($\sim$150 km^2). This study covered a 6-yr period (1999–2004) and consisted of over 50 000 footprints for each GV site. In the first analysis, the results showed that all of the respective rain-rate estimates agree well, with some exceptions. The more salient differences were associated with heavy rain events in which one or more of the algorithms failed to properly retrieve these extreme events. Also, it appears that there is a preferred mode of precipitation for TMI rain rates at or near 2 mm h^{-1} over the ocean. This mode was noted over ocean areas of Kwajalein and Melbourne and has been observed in TRMM tropical–global ocean areas as well.

1. Introduction

The Tropical Rainfall Measuring Mission's (TRMM) Ground Validation (GV) program was established early in the prelaunch phase of the mission with the principal long-term goals of determining the accuracy of the satellite rainfall measurements and the systematic biases stemming from application of the rainfall algorithms. More specifically, the GV program was structured around two validation strategies: 1) determining the quantitative accuracy of the integrated monthly rainfall products at GV regional sites over large areas of about 500 km^2 using integrated ground measurements and 2) intercomparing–validating instantaneous satellite and GV rain-rate statistics at spatiotemporal scales optimized to the various resolutions of the satellite and GV sensors (Simpson et al. 1988; Thiele 1988). This study will address both parts of the validation problem, but will primarily be concerned with validating the instantaneous satellite rain products.

The GV program was originally designed around validating the TRMM Microwave Imager (TMI), Precipitation Radar (PR), and Combined (COM) standard rain products on monthly scales over the regional GV sites. Prior to launch, instantaneous validation was still considered somewhat intractable because of statistical uncertainties stemming from the spatiotemporal measuring characteristics of the satellite and GV observations. Direct instantaneous comparisons between coincident measurements are difficult to achieve without a sufficient number of regional overpasses. But empirically verifying the accuracy on monthly time scales using independent datasets at the surface has also posed logistical challenges due to the existence of temporal sampling errors in the integrated rain estimates.

The TRMM satellite retrieves rain information between roughly 35°N and 35°S while orbiting over the surface of the earth. The satellite collects between one and three estimates per day over any given location

Corresponding author address: David B. Wolff, NASA/GSFC, Code 613.1, Greenbelt, MD 20771.
E-mail: wolff@radar.gsfc.nasa.gov

DOI: 10.1175/2008JAMC1875.1

© 2008 American Meteorological Society

within its sampling domain depending on the latitude of the orbit. Monthly rain estimates on regional scales are subsequently determined statistically from the mean rain rate inferred from all the observations collected in a given month at the resolution of the gridded level III rain products. This sampling strategy results in a statistical mixing of the sampling and retrieval errors in the integrated rainfall products (Bell and Kundu 1996; Bell and Kundu 2000; Bell et al. 2001; Steiner et al. 2003; Fisher 2007).

Various studies have shown that the sampling errors explain at least 8%–12% of the variance between monthly satellite and GV rain estimates (Laughlin 1981; Shin and North 1988; Bell et al. 1990; Oki and Sumi 1994; Fisher 2004, 2007). This significant contribution to the total error budget at monthly scales complicates our determination of the accuracy of the satellite rain algorithms, since the connection between the instantaneous measurement and the rain estimate is to some extent lost in the statistical integration.

This study uses 6 yr (1999–2004) of satellite overpasses of the GV site for comparison with coincident TRMM rain intensity estimates. The data are pixel matched in both time and space, and statistics are provided for comparing GV rain intensities (derived via ground-based radars and rain gauges) to the three principal estimates from the TRMM satellite (PR, TMI, and COM algorithms). The instantaneous matching is performed at 0.5° × 0.5° using a gridded level-III product (3G68) and at 150 km using TRMM level-II products that provide rain rates along the orbital track. By performing these comparisons on an instantaneous scale, we are able to remove a large source of uncertainty in the satellite estimates.

2. Data sources

a. TRMM GV

The GV program operationally produces quality controlled rainfall products for four primary sites: Darwin, Australia (DARW); Houston, Texas (HSTN); Kwajalein, Republic of the Marshall Islands (KWAJ); and, Melbourne, Florida (MELB). These sites were established during the premission phase of TRMM, providing researchers with a quasi-continuous, long-term time series of rainfall measurements at a higher spatiotemporal resolution than can be observed with the satellite sensors alone. The GV data provide an empirical surface reference needed to independently verify the accuracy of TRMM measurements of rainfall (Thiele 1988).

The GV program is documented in Wolff et al. (2005), including site and product descriptions, as well as algorithms and data processing techniques. For this study, we used the TRMM 2A53 instantaneous rain maps that are distributed to the scientific community through the Goddard Earth Sciences Data and Information Services Center (GES-DISC). The 2A53 data provide instantaneous rain rates at a resolution of 2 km × 2 km and cover a continuous region extending 150 km from the given GV radar. Each rain map thus consists of a 151 × 151 pixel grid with the GV radar located at the center pixel.

Geographical maps of the gauge and radar networks at DARW, HSTN, KWAJ, and MELB are provided in Fig. 1. The maps in Fig. 1 illustrate one of the key operational dilemmas of TRMM GV: principally ocean sites, such as KWAJ, that provide the most physically robust comparisons for passive microwave (PM) retrievals provide only limited real estate for deployment of gauges that can be used for calibration and validation of the GV radar rainfall estimates. On the other hand, sites with substantial gauge coverage such as DARW, HSTN, and MELB lack extensive ocean coverage and contain significant coastal areas over which it is inherently difficult, if not impossible, for PM algorithms to robustly estimate rain intensities. Although it is well known that there are problems with current PM physical algorithms in coastal areas, we will show that the full-GV-area probability distributions of rain rates are dominantly affected by coastal algorithm uncertainties, and comparison to or validation of TRMM estimates without removing estimates near coastlines are doomed to failure, or at the very least, misinterpretation.

Figure 2 provides another depiction of the GV sites, illustrating the land–coast–ocean 1/6° terrain mask used by the version-6 TMI algorithm to delineate geographical type: dark gray is "ocean," medium gray denotes "coast" (both coastal land and coastal water), and light gray denotes "land." Also shown are the more subjectively classified terrain types within each of the 0.5° grid locations of the TRMM 3G68 product, employed in this study. In these figures, "L" is for land, "C" for coast, and "O" for ocean. Additionally, a GV coverage notation is provided ("F" for full coverage and "P" for partial). The purpose of the coverage flag is to identify pixels that are both fully observed by the GV radar (i.e., ranges between 15 and 150 km) and that contain a supermajority of one geographical type (i.e., mostly ocean, coast, or land, subjectively set at about 60%). For this study, only the F pixels were considered.

b. TRMM satellite: TMI and PR rain sensors

The TRMM satellite was launched on 27 November 1997 into a sun-asynchronous, low-earth orbit at an al-

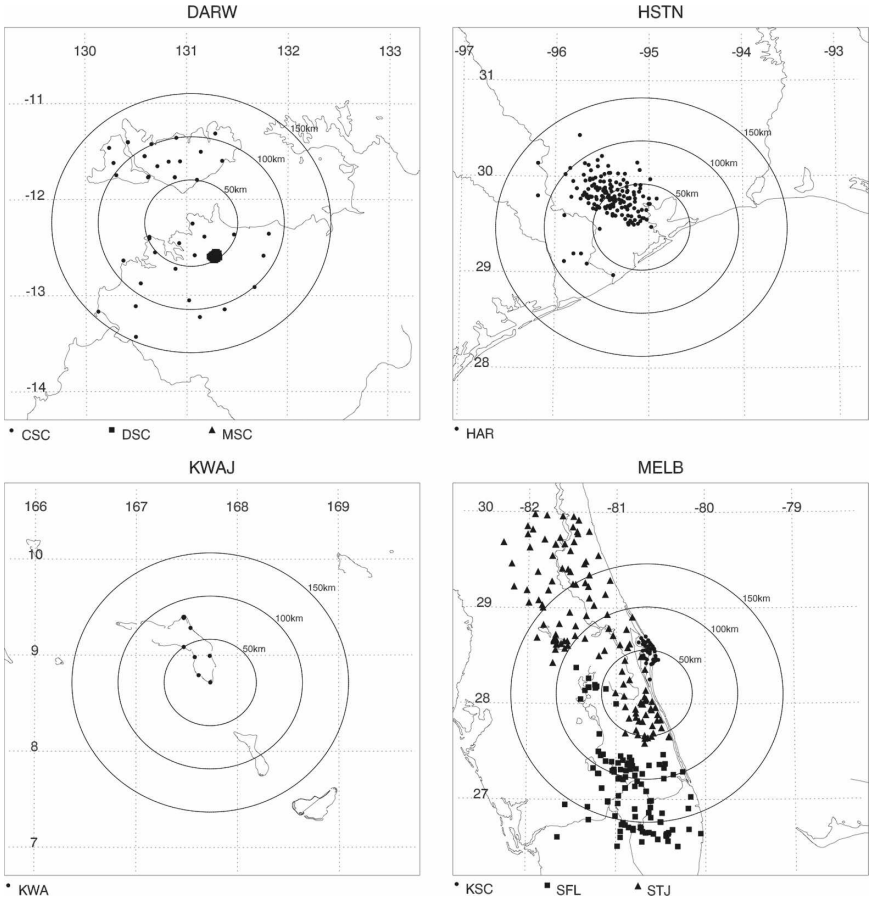

FIG. 1. Map illustrating the gauge and radar networks at the GV sites: Darwin, Australia (DARW); Houston, TX (HSTN); Kwajalein, Republic of the Marshall Islands (KWAJ); and Melbourne, FL (MELB). Rings show distances from GV radar at increments of 50 km. The symbols in the figures correspond to the operational gauge networks shown below each panel.

titude of 350 km. In August 2001, the satellite was repositioned from an average altitude of 350 km to 402 km. This orbital adjustment was made in order to conserve fuel and to extend the life of the mission. Global analyses of instantaneous TMI and PR rain rates indicate that the boost only had a marginal effect on the TMI rain rates, but on average, PR rain rates appear to have been lowered. Systematic changes in the PR rain rates due to the boost are still being investigated (J. Kwiatkowski, NASA GSFC, 2006, personal communication).

The satellite instrument package described by Kummerow et al. (1998) includes a dual complement of passive and active rain sensors—the TMI and PR—that collect rain information using different remote sensing techniques. The TMI passively collects rain information using nine channels at five microwave frequencies: 10.7, 19.4, 21.3, 37.0, and 85.5 GHz. The 21.3-GHz channel is the only one that is not dually polarized (only the vertical channel is available at 21.3 GHz). The PR is the first space-borne radar used in the collection of rain observations. The PR operates at a frequency of 13.8 GHz and has a minimum sensitivity of about 17 dBZ ($\sim$0.25 mm h^{-1}). The sensor's horizontal and vertical resolutions near nadir are about 4.3 km and 250 m, respectively. Its superior vertical and horizontal resolution allows the PR to observe smaller-scale precipitation features that cannot be unambiguously resolved by the TMI (Kummerow et al. 1998).

At 13.8 GHz (2.17-cm wavelength), the PR is strongly attenuated by intervening rain. To account for this reduction in the observed return signal, a path attenuation correction is applied to the measured reflectivity using the surface reference technique (SRT). This methodology generates an effective reflectivity factor that is used in the subsequent estimation of surface and near-surface rain rates (Iguchi et al. 2000; Meneghini et al. 2000). The SRT naturally constrains the PR field of

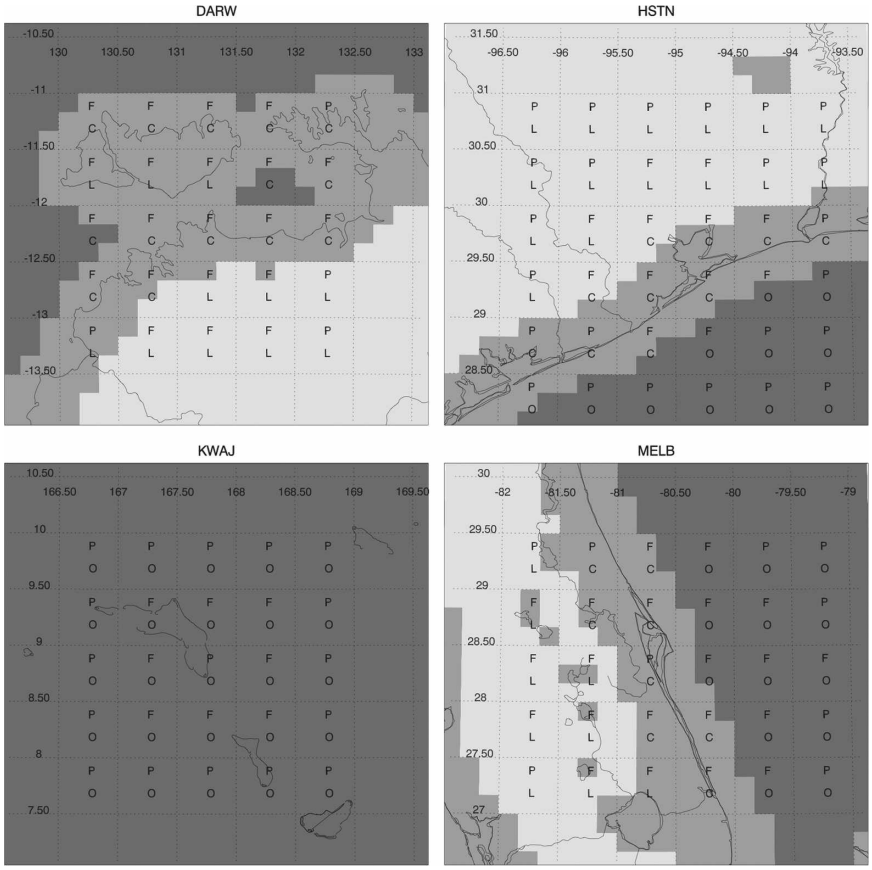

FIG. 2. Illustration of land–coast–ocean 1/6° mask used by the v6 TMI algorithm for each GV site. Shaded regions show the TMI v6 surface masks of land (dark gray), coast (medium gray), and ocean (light gray). Also shown are the more subjectively classified 0.5° × 0.5° grids used for comparison of the GV data with the TRMM 3G68 product. The first letter in each grid box designates the GV coverage (F denotes full GV coverage, P is for partial), and the second letter designates the terrain type: L, land; C, coast; and O, ocean. Only areas with full GV coverage are used in this study.

view (FOV) to a narrow cross-track swath of 250 km (i.e., cross-track scanning angles within 17° of nadir). The attenuation correction can be a significant source of error in heavy rainfall.

c. *TMI rain algorithm with respect to ocean, land, and coastal classification*

The TMI operational algorithm is well documented in the literature and a complete physical description is considered beyond the scope of this paper, but for the purpose of this study it is important to note some of the differences that exist between the land, coastal, and ocean algorithms in the generation of rain rates from microwave radiances. Also, unless otherwise stated, we will utilize the TRMM version 6 data in our comparisons with GV data. While there are inherent differences in the actual distribution of rainfall over land and ocean, much of the intrasatellite variance between the TRMM estimates over ocean and land is due to the physical assumptions and intrinsic uncertainties of the retrieval algorithms.

The Goddard profiling (GPROF) algorithm estimates instantaneous TMI rain rates over the ocean, land, and coast using precipitation information obtained remotely from the observed emissions and scattering of hydrometeors in the atmosphere. The information collected in all nine channels provides a radiometric temperature sounding at different depths of the precipitating cloud (Kummerow et al. 1998). To estimate the cloud liquid water content, the rain signal needs to be distinguished from the microwave background upwelling from the surface. This is most easily accomplished over the radiometrically cold oceans, which cover three-quarters of the earth's surface. Over

the oceans, GPROF applies a physical algorithm utilizing the radiometric information of all nine TMI channels (Kummerow et al. 1996, 2001).

The algorithm first applies a radiative transfer model to compute an observed brightness temperature profile from the rain information in each of the channels. The observed brightness temperature profile is next compared to a large database of cloud radiation model simulations, which locates the simulated cloud profile that results in the best match (Tau and Simpson 1993; Olson et al. 2006). The algorithm then employs a simple inversion methodology using Bayes's probabilistic theorem to determine the rain-rate profile, R, given a brightness temperature profile Tb:

$$\Pr(R|\mathrm{Tb}) = \Pr(R) \times \Pr(\mathrm{Tb}|R), \tag{1}$$

where $\Pr(R)$ is the probability that a certain profile R will be observed and $\Pr(\mathrm{Tb}|R)$ is the probability of observing the brightness temperature vector Tb, given a particular rain-rate profile.

The rain retrievals are considerably more complicated over the radiometrically warm land surface due to variations in soil moisture, vegetation and transpiration, and surface roughness and topography. So far, the difficulty in handling the microwave background over land has precluded the usage of the lower-frequency emission channels. Spencer et al. (1989) showed that at 85.5 GHz a reduction in the detected signal related to the scattering of radiation from frozen hydrometeors above the freezing level can be used as an empirical estimator of rain rate. Rain rates over land are subsequently determined empirically from the scattering information in the two 85.5-GHz channels (Spencer et al. 1989; Ferraro 1997; Conner and Petty 1998; McCollum and Ferraro 2003). However, brightness temperature–rain-rate relations are not directly related to surface rainfall, since they characterize scattering processes in the higher regions of the cloud (Wilheit et al. 2003). Currently, GPROF applies an empirically based rain algorithm originally developed by Ferraro (1997) and McCollum and Ferraro (2003).

The problems over land are further exacerbated around coastal regions due to the sharp contrast between land and ocean surfaces of the TMI footprint. In this case, the radiometrically warm land and cold ocean surfaces are both present in the TMI footprint. Coastal pixels are treated using a decision tree that first determines whether rain exists in the pixel. If a determination of rain existence cannot be made, then the pixel is classified as ambiguous and a rain rate is not assigned. If rain exists, then the rain rate is determined using empirical relations described in McCollum and Ferraro (2005) and others.

d. The Combined (COM) algorithm

A full and complete description of the COM algorithm is beyond the scope of this paper, but generally the algorithm estimates the mean rain rate and confidence bounds by combining the rain information from both the TMI and PR. The COM algorithm is based on the idea that combining the rain information from both sensors would result in a more accurate product than either of the two sensors alone by taking advantage of the relative strengths of each measurement.

The COM algorithm also takes a Bayesian approach to produce the best estimates of the mean rain rate and the variance (i.e., uncertainty in the estimate). The methodology is performed in three steps. Using a joint probability distribution for the drop size distribution (DSD) and shape parameters, the first step of the procedure applies the radar inversion equation to generate an estimate of the mean rain rate and variance for the PR. The joint probability distribution conditionally based on the radar measurements is then used to predict a corresponding mean brightness temperature for the TMI. A joint probability distribution conditioned on both radar and TMI is then generated. The conditional mean of the distribution quantifies the best estimate of the rain rate, while the standard deviation provides an estimate of the uncertainty.

e. TMI, PR, and COM datasets

For this study, we used two different datasets for comparison, both representing version 6 TRMM data. The first, a gridded product known as 3G68, provides area rain averages in $0.5° \times 0.5°$ latitude–longitude boxes for the TMI, PR, and COM algorithms. For the second set of comparisons, we utilized the TRMM level II footprint data obtained from the satellite-coincidence subsets of the 2A12 (TMI), 2A25 (PR), and COM (2B31) products, and then calculated all statistics at the scale of each individual footprint observed by the TMI that was within the PR- and GV-viewable ranges of the respective GV site.

Table 1 provides the percentage of land, coast, and ocean areas for different geographical regions, along with the four primary TRMM GV sites. The "TRMM" area is defined as being from 35°N to 35°S and represents the satellite's sampling domain, while the "deep tropics," a subset of this region, is defined as being between 10°N and 10°S. Table 1 shows that all of the GV sites listed, except KWAJ, contain significant coastal areas; the rain rates inferred for the pixels classified as coast have the greatest amount of uncertainty, for reasons that were described previously. For brevity,

TABLE 1. The number of 1/6° pixels and percentages (in parentheses) of geographical types, via the TRMM TMI v6 algorithm, as a function of sampling area: global represents ±70° latitude, TRMM area is ±35° latitude, and deep tropics is ±10°. Also shown are the respective percentages of the geographical types at the four GV sites. Note that all GV sites except KWAJ have a significant percentage of coastal pixels, limiting the usefulness of the comparisons to passive microwave estimates.

Area	Ocean	Land	Coast	Other	Total
Global	952 643 (40.8)	682 813 (29.3)	154 289 (6.6)	543 055 (23.3)	2 332 800
TRMM	646 298 (71.2)	217 582 (24.0)	43 044 (4.7)	276 (0.0)	907 200
Deep tropics	191 754 (74.0)	51 275 (19.8)	16171 (6.2)	—	259 200
KWAJ	441 (100.0)	—	—	—	441
MELB	112 (41.5)	72 (26.7)	86 (31.9)	—	270
HSTN	90 (27.8)	153 (47.2)	81 (25.0)	—	324
DARW	104 (27.5)	104 (27.5)	170 (45.0)	—	378

we will provide detailed comparisons of our GV estimates over KWAJ and MELB.

KWAJ is essentially an open-ocean site and most suitable for validating the TMI ocean estimates in which all rain information is utilized from the nine TMI channels. MELB, in contrast, is located in the subtropics and has a rain climatology that is dominated by isolated convection and tropical cyclones. As can be seen in Table 1, MELB has a good distribution of land, ocean, and coastal pixels.

3. Comparisons of 0.5° × 0.5° gridded data

In section 3a, TMI, PR, and COM rain rates are intercompared over monthly, annual, and 5-yr time periods at a grid resolution of 0.5° × 0.5° to GV rain rates over the GV sites of KWAJ and MELB. Probability density functions (PDF) of the instantaneous rain rates are then constructed in section 3b using all of the data collected over 5 yr for each of the four estimates.

The TMI, PR, and COM rain rates were obtained

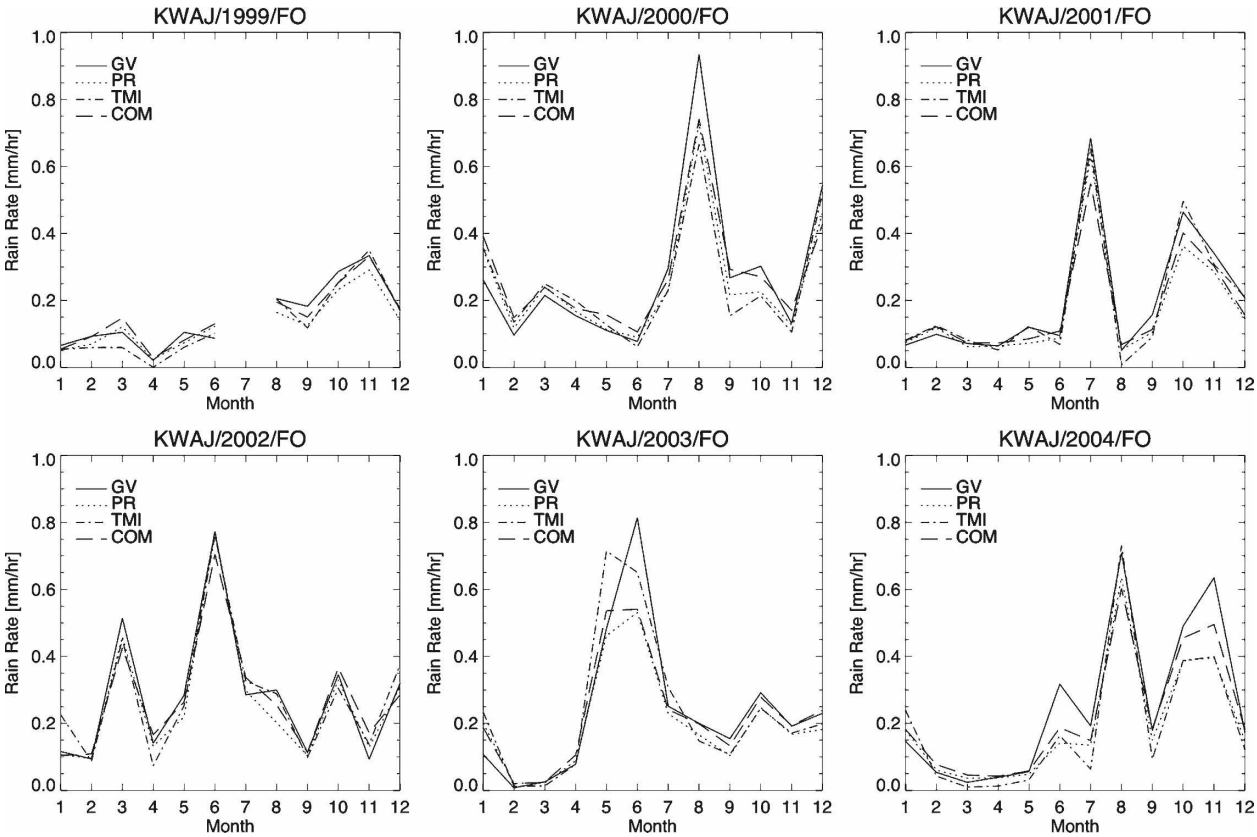

FIG. 3. Mean monthly rain intensities (mm h^{-1}) for GV, PR, COM, and TMI using 0.5° resolution for the period 1999–2004 at KWAJ.

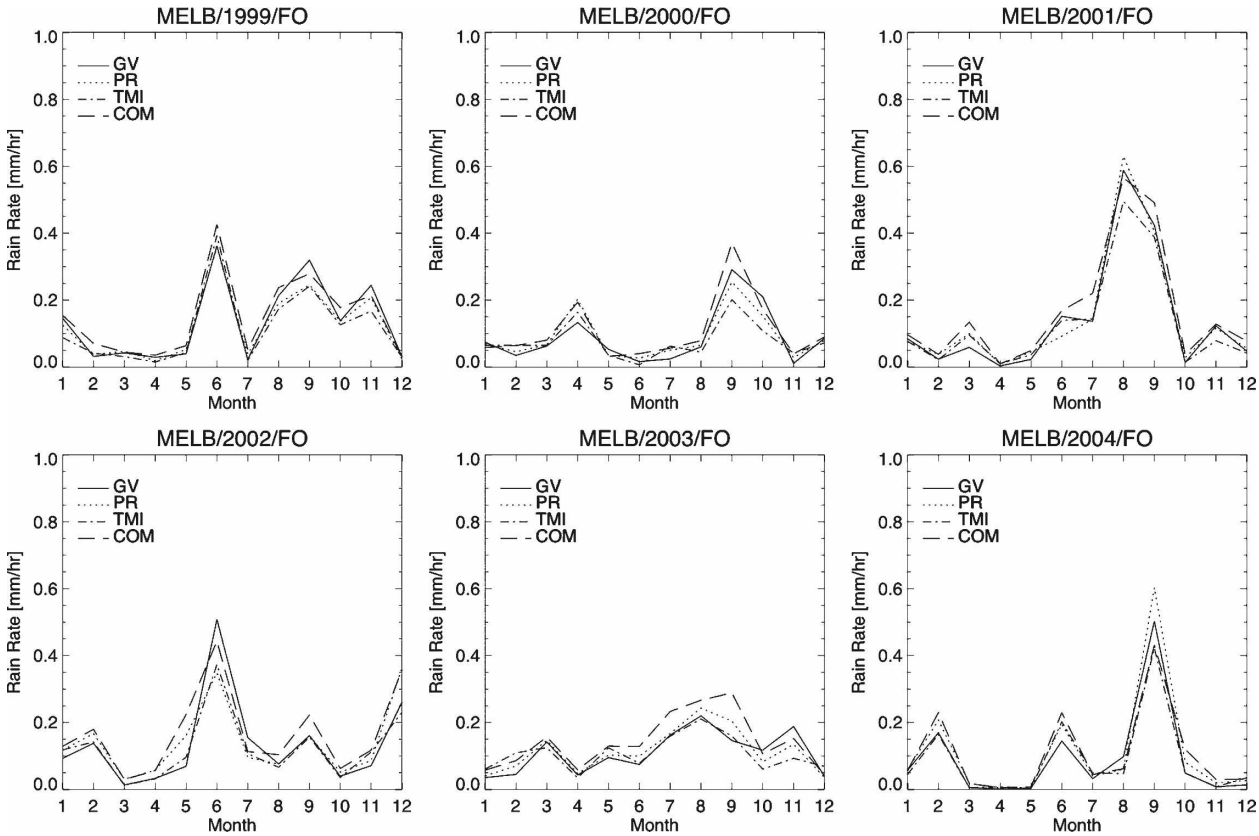

FIG. 4. As in Fig. 3, but for MELB over ocean only.

from the 3G68 instantaneous rain product. This special satellite rain product provides instantaneous, area-averaged rain rates for the TMI, PR, and COM along the orbital track of the TRMM satellite at a grid resolution of 0.5° × 0.5° (Stocker et al. 2001). For this grid spacing, satellite and GV rain rates were matched in both time and space, which effectively mitigated the temporal sampling errors as a source of uncertainty with respect to the noncontiguous sampling of the TRMM satellite. The GV 0.5° × 0.5° gridded rain rates were obtained by averaging the rain rates obtained during TRMM overpasses from the gridded 2A53 product described in section 2.

To provide a more detailed comparison, the data from MELB was further subdivided into land, coast, and ocean categories as defined by the TMI terrain mask (see Fig. 2). We note that only pixels with a coverage type of full (F) were used, and thus the subsets consisted of all pixels designated as either full ocean (FO), full coast (FC), or full land (FL) types. For KWAJ, there are no land or coast pixels: for algorithmic purposes, it is treated as solely oceanic. However, the version 5 (v5) TRMM algorithms considered KWAJ as nearly 40% coast, given the coarse surface-type mask (0.25°) used at that time. The finer-resolution version 6 (V6) TMI surface mask of ~0.166° was also manually modified to exclude classification of small islands and atolls as coastal, prior to the implementation of the V6 algorithm (Olson et al. 2006). In this analysis, all GV rain maps (2A-53) from 1999 to 2004 were used for comparison to the TRMM estimates.

a. Comparison of monthly means of instantaneous rain rates

Figures 3–6 display the mean monthly area rain rates at KWAJ and MELB for each rain-rate product (TMI, PR, COM, and GV) over the period from 1999 to 2004. Table 2 lists the mean rain rates on annual and 6-yr time periods; the last three columns of the table report the associated biases, in percent, for each of the satellite rain rates relative to GV.

The biases in Table 2 are defined via Eq. (2) using the mean GV rain rate as an empirical reference:

$$\text{Bias} = \frac{(\overline{E} - \overline{G})}{\overline{G}} \times 100, \qquad (2)$$

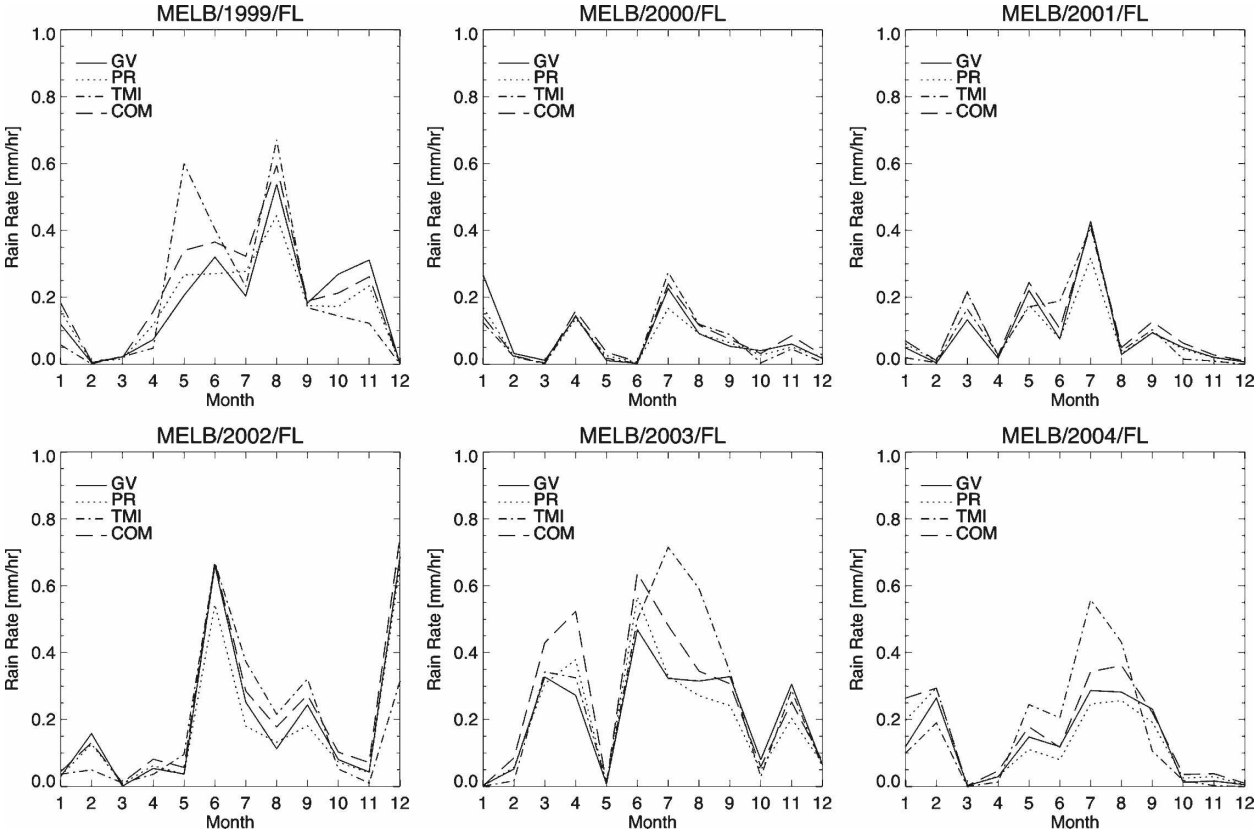

FIG. 5. As in Fig. 3, but for MELB over land only.

where $\overline{E}$ is the mean rain rate of the satellite estimate (PR, TMI, or COM) and $\overline{G}$ is the mean rate from GV. All biases are hereafter referred to in percentages.

The TMI, PR, and COM FO estimates for KWAJ are shown in Fig. 3 and are seen to be in good agreement with GV, with a few notable exceptions observed during August 2000, May–June 2003, and several months in 2004. Refer to Table 2 for specific values of the annual means and the resultant biases. It is observed that the biases reported in Table 2 for KWAJ are predominantly negative. The 5-yr satellite-inferred rain biases were −13.7% (PR), −7.9% (TMI), and −5.7% (COM).

The negative satellite biases at KWAJ are attributed to two systematic sources of error: 1) known calibration issues in the GV radar at KWAJ and 2) an underestimation of the higher rain rates by the satellite algorithms (>20 mm h^{-1}). The variations in the calibration of the KWAJ radar are considered the largest contributor to the monthly biases reported in Table 2. The calibration issues related to the performance of the KWAJ radar are reported by Houze et al. (2004), Marks et al. (2005), and Silberstein et al. (2008). Houze et al. (2004) and Marks et al. (2005) identified sudden changes in the radar's calibration and related them directly to mechanical and engineering issues (e.g., replacement of parts) that arose during the study period. These calibration offsets were not taken into account in the v5 2A53 rain products. In conjunction with ongoing research and development for TRMM GV, Silberstein et al. (2008) have developed and tested a new methodology for correcting these problems, known as the relative calibration adjustment (RCA). The RCA uses a large sample of points in the radar's clutter field to both identify when calibration changes occur and determine the magnitude of the change; the methodology is currently undergoing final testing for use in the generation of the version 7 (v7) 2A53 products.

The systematic underestimation of the higher rain rates by the TMI and PR, in the case of KWAJ, is not as significant as the calibration offsets, but also contributes to the negative biases observed in Table 2. Moreover, an underestimation of rain rates at the high end of the rain-rate spectrum was also observed in the case of MELB where the calibration has been stable over time. The algorithm issues associated with the determination of higher rain rates by the TMI and PR for KWAJ and MELB will be investigated in more detail in section 4 in conjunction with the footprint analysis of the instantaneous rain rates.

For MELB, the data were stratified into ocean (FO),

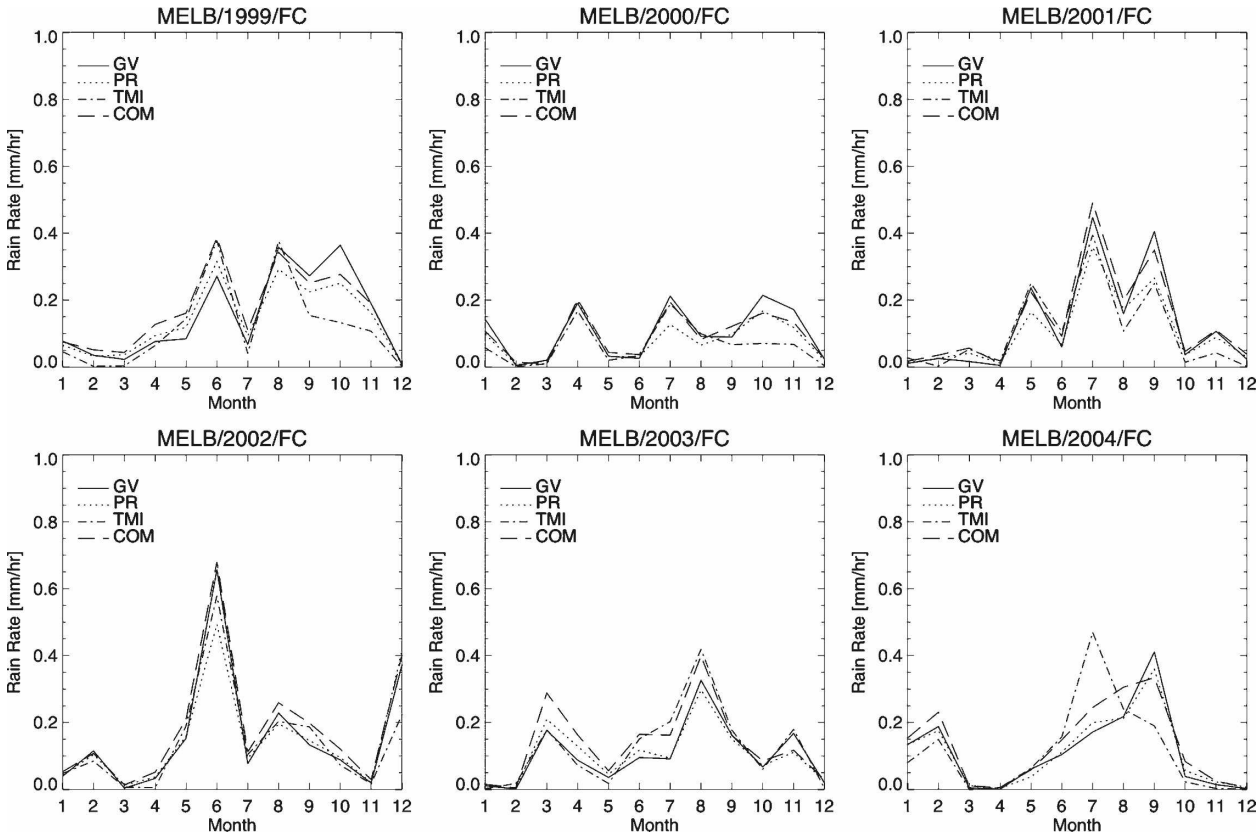

FIG. 6. As in Fig. 3, but for MELB over coast only.

land (FL), and coast (FC) categories. The monthly rain rates for each case are displayed in Figs. 4–6, respectively. The FO satellite and GV mean monthly rain rates shown in Fig. 4 exhibit good agreement but there are some notable disagreements, especially during peak rainfall months. In Table 2, the PR annual bias, relative to GV, is positive in 5 out of 6 yr while the COM is positive in all 6 yr. The TMI FO biases, on the other hand, are negative for each of the 6 yr. In general, the peak rainfall months contribute the bulk of the annual biases shown in Table 2.

In contrast with the FO case, the PR biases over coast and land are predominantly negative. The TMI land bias, on the other hand, is more variable and was positive in 4 out of 6 yr, whereas it was negative for all 6 yr in the ocean case. This observation is also consistent with the overall 6-yr biases, which in the FL case were +10.2% and −8.1% in the FO case. Over the coast, the TMI FC bias tended to be negative, but with year-to-year results covering a broad range between −34.9% and +18.5% over the 6-yr study period. These results pointedly reflect the differences in the TMI algorithm for each of the three terrain cases.

The COM bias is positive in 5 of 6 yr for both FL and FC, with 5-yr biases of 18.4% and 13.9%, respectively. An examination of Figs. 5 and 6 reveals that the bulk of the annual biases displayed in Table 2, as noted earlier, can be related to contributions during the peak rain periods, most notably during the months of May–September. The rainfall climatology of central Florida is an important factor in evaluating the performance of the satellite algorithms. The rainfall budget during the summer months is dominated by sea-breeze-generated isolated convection, as well as mesoscale and synoptic-scale rain systems and tropical cyclones. A more detailed examination of the instantaneous rain-rate spectrums for the TMI, PR, COM, and GV will be presented in section 4.

b. *Probability distributions of instantaneous rain rates*

The PDFs of the TMI, PR, COM, and GV estimates constructed at the 0.5° scale are difficult to compare due to the inherent noise given the somewhat limited sample size; however, the cumulative distribution functions (CDF) do provide additional insight into the comparisons. Figure 7 illustrates the PDF and CDF plots for KWAJ. In Fig. 7, the GV, PR, TMI, and COM distri-

TABLE 2. Statistics for the 3G68 comparison of KWAJ and MELB showing site, year, and mean rain rates (GV, PR, TMI, and COM), as well as the GV-relative biases. All bias values are expressed in percentages.

Site	Year	Type	GV mean	PR mean	TMI mean	COM mean	PR bias	TMI bias	COM bias
MELB	1999	FL	0.1923	0.1806	0.2069	0.2239	−6.1	7.6	16.4
MELB	2000	FL	0.0838	0.068	0.0743	0.0822	−18.9	−11.3	−1.9
MELB	2001	FL	0.0971	0.093	0.0993	0.1175	−4.3	2.2	21.0
MELB	2002	FL	0.1814	0.1582	0.1766	0.2052	−12.8	−2.6	13.1
MELB	2003	FL	0.2194	0.2142	0.2778	0.2769	−2.4	26.6	26.2
MELB	2004	FL	0.1266	0.1228	0.1538	0.1592	−2.9	21.5	25.8
MELB	**1999–2004**	**FL**	**0.1516**	**0.1409**	**0.167**	**0.1795**	**−7.0**	**10.2**	**18.4**
MELB	1999	FC	0.1541	0.1426	0.1232	0.1705	−7.4	−20.0	10.7
MELB	2000	FC	0.1038	0.0817	0.0675	0.0956	−21.2	−34.9	−7.8
MELB	2001	FC	0.1256	0.1034	0.1054	0.1366	−17.7	−16.1	8.7
MELB	2002	FC	0.1542	0.1454	0.1412	0.181	−5.7	−8.4	17.4
MELB	2003	FC	0.1079	0.1106	0.1279	0.144	2.5	18.5	33.4
MELB	2004	FC	0.1135	0.1113	0.1136	0.1336	−1.9	0.1	17.7
MELB	**1999–2004**	**FC**	**0.1263**	**0.1161**	**0.1139**	**0.1439**	**−8.1**	**−9.9**	**13.9**
MELB	1999	FO	0.1369	0.1254	0.1164	0.1506	−8.4	−15	10.1
MELB	2000	FO	0.0873	0.089	0.0774	0.1046	2.0	−11.4	19.9
MELB	2001	FO	0.1199	0.1232	0.1118	0.1504	2.7	−6.8	25.4
MELB	2002	FO	0.13	0.1363	0.1194	0.164	4.9	−8.1	26.2
MELB	2003	FO	0.1098	0.1153	0.1071	0.1426	5.0	−2.5	29.8
MELB	2004	FO	0.0918	0.1115	0.087	0.1058	21.5	−5.1	15.4
MELB	**1999–2004**	**FO**	**0.1124**	**0.117**	**0.1032**	**0.1364**	**4.1**	**−8.2**	**21.3**
KWAJ	1999	FO	0.1651	0.1392	0.1459	0.1603	−15.7	−11.6	−2.9
KWAJ	2000	FO	0.2881	0.2571	0.2536	0.2817	−10.8	−12.0	−2.2
KWAJ	2001	FO	0.2149	0.1816	0.2071	0.1884	−15.5	−3.6	−12.3
KWAJ	2002	FO	0.2807	0.2621	0.2804	0.2744	−6.6	−0.1	−2.3
KWAJ	2003	FO	0.2379	0.2039	0.2431	0.2268	−14.3	2.2	−4.6
KWAJ	2004	FO	0.2269	0.174	0.1642	0.2027	−23.3	−27.6	−10.7
KWAJ	**1999–2004**	**FO**	**0.2383**	**0.2055**	**0.2194**	**0.2247**	**−13.7**	**−7.9**	**−5.7**

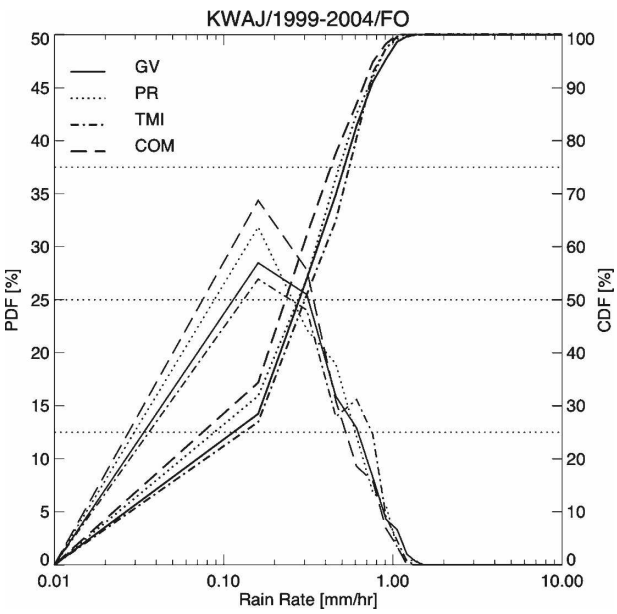

FIG. 7. PDFs (curves with peaks near 0.04 mm h^{-1}) and CDFs of instantaneous rain rates (0.5° resolution) for GV, PR, COM, and TMI as inferred from 3G68 products using 0.5° resolution for the period 1999–2004 at KWAJ.

butions are provided. Also shown are the upper and lower quartiles and median rain rates for the estimates (thin horizontal dotted lines). At KWAJ, the COM rates are consistently lower than the other estimates, with a median of about 0.55 mm h^{-1}, while the TMI rain rates are generally higher than the other estimates with a median of about 0.7 mm h^{-1}. The PR and GV distributions agree well with medians of about 0.6 mm h^{-1}.

Figure 8 provides the PDFs and CDFs at MELB for FO, FC, and FL pixels, in the left, middle, and right panels, respectively. Over ocean, the CDFs agree quite well, with median rain rates differing by less than 1 mm h^{-1}. Over coastal pixels, the scatter among the CDFs is more evident, showing better agreement between the PR and TMI estimates, which are both lower than the GV and COM estimates. In general, the GV distributions fall within the bounds of the other distributions. Over land, there is better agreement between the estimates than over coast areas. Also, over land, the PR rain rates are less than the other estimates, while the TMI and GV rates are quite similar.

In summary, our 0.5° gridded comparisons of the data show that there is good agreement between the

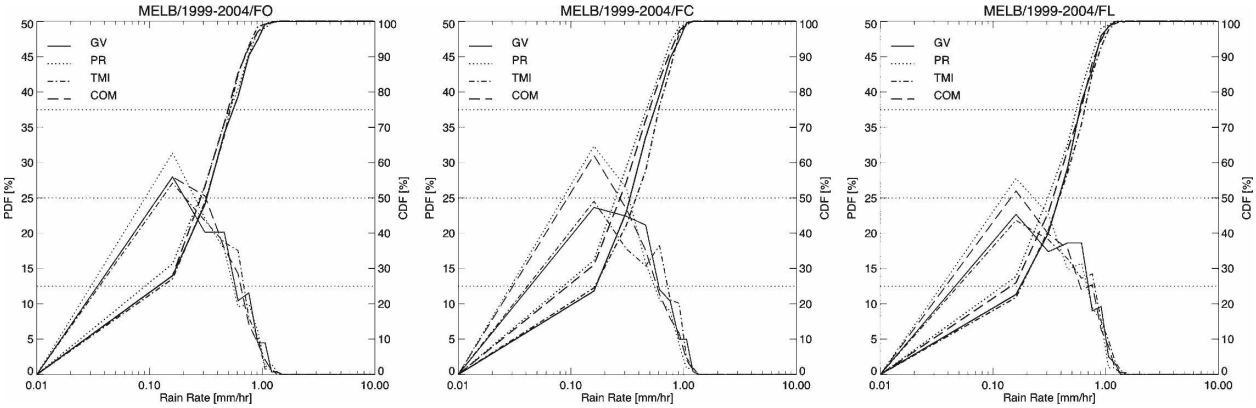

FIG. 8. As in Fig. 7, but for MELB over (left) ocean, (middle) coast, and (right) land.

various estimates, and that there are no systematic biases shown between one estimate versus the others. The discrepancies that do occur are associated with specific (heavy) precipitation events; however, overall the near-decade-long TRMM products, and the GV estimates to which they are compared, are quite robust and provide a unique dataset for future study of precipitation physics and climate analyses.

4. Validation at the TMI footprint scale

a. Description of analysis

The primary emphasis of the GV validation program in the early years of TRMM was on verifying the accuracy of the level-III monthly products at planned GV sites using well-calibrated surface-based rain sensors. The validation strategy employed was to characterize the errors in the satellite rain products used in climate-scale applications at an averaging scale that minimized the space–time uncertainties between surface and satellite sensors (Thiele 1988). In addition to the obvious interest in quantifying the error bounds in the higher-level TRMM products, there was also interest in using the GV data to assess the accuracy of the TRMM level-II instantaneous rain products at the fundamental resolution of the satellite sensors (i.e., the footprint scale), for instantaneous validation provides a more direct physical probe of the systematic errors in the operational rain algorithms.

Validation at instantaneous scales, perhaps most importantly, eliminates the temporal sampling error from consideration. Previous studies of the temporal sampling error—the error associated with the discreet regional sampling of the satellite—have shown that it can account for up to 25% of the variance between satellite and ground estimates on monthly scales (Laughlin 1981; Oki and Sumi 1994; Bell and Kundu 1996; Bell et al. 2001; Steiner et al. 2003; Fisher 2004, 2007). But even given coincident, instantaneous observations on larger scales (e.g., TRMM 3G68), small-scale discrepancies between satellite rain products due to interalgorithmic differences can become "smoothed out" in the averaging process, limiting the usefulness of such comparisons. Random errors, in turn, increase substantially as the time–space averaging scale is reduced to the footprint scale, due to navigational uncertainties between GV and satellites and differences in the measuring characteristics of the sensors.

In this part of the study, level-II TMI, PR, and COM instantaneous rain rates were matched at the scale of the TMI footprint and were statistically compared with the level-2A53 GV radar-rain rate spectrums at both KWAJ and MELB. Six years of regional TRMM overpass data were used (1999–2004). As seen in Table 3, the available data provided a large sample of more than 50 000 TMI footprints for each GV site, with each TMI footprint covering an area of about 150 km^2. Though the TMI "footprint" used in this study provides a convenient scale for analysis, it does not represent a fundamental physical scale since the size is determined based on an empirical optimization of rain information spanning a broad spectrum of physical scales and 13.9-km along-track sampling resolution (Kummerow et al. 1998; Olson et al. 2006). The effective field of view at 10 GHz for example is 67 $\times$ 37 km^2, whereas at 85 GHz the field of view is 7 $\times$ 5 km^2 (the level-II TMI foot-

TABLE 3. Number of TRMM overpasses and associated TMI footprints available for this study over the period 1999–2004, for each GV site.

GV site	No. of overpasses	No. of footprints			
		All	Ocean	Land	Coast
KWAJ	257	70 993	70 993	0	0
MELB	236	54 943	16 875	16 618	21 450

print, in effect, undersamples the low-frequency channels and oversamples the high-frequency channels). The TMI footprint here represents a kind of maximum sample spacing; in other words, if one lay 14 km × 14 km boxes centered on each TMI radiance footprint, they would be spatially contiguous from scan to scan, but overlap along the scan line.

The swaths of the TMI and the PR sensors along TRMM's orbital track represent the sampling domain of the satellite. The GV sampling domain of the radar encompasses a circular domain extending 150 km from the radar location. For this analysis, the instantaneous rain-rate information was restricted to the geographical intersection of the TMI and PR orbital track within the GV radar domain. Figure 9 displays four instantaneous snapshots for the GV, TMI, PR, and COM rain-rate estimates for TRMM orbit 01707 on 7 October 1999 over KWAJ, in the top-left, top-right, bottom-left, and bottom-right panels, respectively. These images illustrate the rain rates at the characteristic or native resolution of each of the respective estimates. The red and blue dashed lines illustrate the edges of the orbital track of the PR.

To simplify the procedure, we matched the TMI, PR, COM, and GV at the scale of the TMI footprint by considering a 7-km radius around the center of the TMI pixel location. Unconditional mean rain rates (i.e., rain rate ≥ 0) were then computed for the GV, PR, and COM at the TMI footprint scale by locating all of the pixels (rainy and nonrainy) found within this circular region. Figure 10 illustrates the same instantaneous snapshots as Fig. 9, but after the GV, PR, and COM rain rates were averaged within the respective TMI footprint areas.

The numbers of GV, PR, and COM pixels associated with each TMI footprint vary from case to case, but tend to average about 8 for PR and COM (native resolution of approximately 4.3 km × 4.3 km $\cong$ 18.5 km^2 resolution) and about 36 for the GV (native resolution of 2 km × 2 km = 4 km^2 resolution). The TMI surface flag was also recorded for each set of matching pixels according to whether the TMI pixel was labeled ocean, land, or coast, as described previously. Table 3 gives a summary of the number of overpasses and the number of footprints for each of the four GV locations and lists both the total number of footprints and the number of footprints in each terrain category (O, L, C) used in this analysis.

b. Footprint statistics: Mean rain-rate profiles

Using the GV matching rain rates as an empirical reference, mean rain-rate profiles were generated for the TMI, PR, and COM spanning a dynamic range between 0 and 40 mm h^{-1}. The profiles were constructed by first binning the instantaneous rain rates matched at each TMI pixel for all four products at 1 mm h^{-1} intervals with respect to the GV rain rate. For example, if the GV rain rate for a given TMI pixel was 5.5 mm h^{-1}, the TMI, PR, and COM rain rates were included in the 5–6 mm h^{-1} bin. The satellite rain-rate information was therefore sorted with respect to the GV rain-rate continuum. The GV profile in subsequent comparisons has by definition a slope of 1. The data in each separate bin were then averaged, after which a 3 mm h^{-1} ($\pm$ 1 mm h^{-1}) mean filter was applied across the entire spectrum. The application of a mean filter was mainly required to increase the effective sample sizes in the higher bins (>20 mm h^{-1}).

Figures 11 and 12 show mean rain-rate profiles constructed for KWAJ and MELB, respectively. In Fig. 12, for MELB, in addition to plotting a mean profile for all the data combined (top left), three additional profiles are shown that subdivide the data according to the TMI terrain surface flag (O, L, or C).

A regression analysis was carried out on each of the profiles shown in Figs. 11 and 12 by splitting the rain-rate spectrum into two equal sectors, designated as high and low rain-rate regimes. The "low" and "high" regimes were defined from 0 to 20 mm h^{-1} and from 21 to 40 mm h^{-1}, respectively. The regression parameters listed in Tables 4 and 5 will be referred to in the following analysis to help illustrate the differences between the two parts of the spectrum.

In general, Figs. 11 and 12 for KWAJ and MELB show good correspondence between the TMI, PR, and COM with GV, in the lower regions of the rain-rate spectrum. The correspondence is considerably less in the higher region of the spectrum, with the COM showing the best agreement with respect to GV. Although the higher rain rates represent an important region of the spectrum—because of their association with convective rain processes—the sample sizes in each bin are considerably smaller and, thus, to some extent their contribution to the total integrated rainfall is lessened. Of course, since the data were spatially averaged at the scale of the TMI footprint, it is not surprising that there are significantly fewer rain-rate samples in the high regime in the cases of the PR and COM (>20 mm h^{-1}).

In the lower rain-rate regime, the linear correlation coefficients between GV and the satellite rain products presented in Tables 4 and 5 are seen to be consistently high ($\rho \geq 0.95$) for both KWAJ and MELB. In the high rain-rate regime, the correlations drop off substantially with large nonzero intercepts along with lower slope

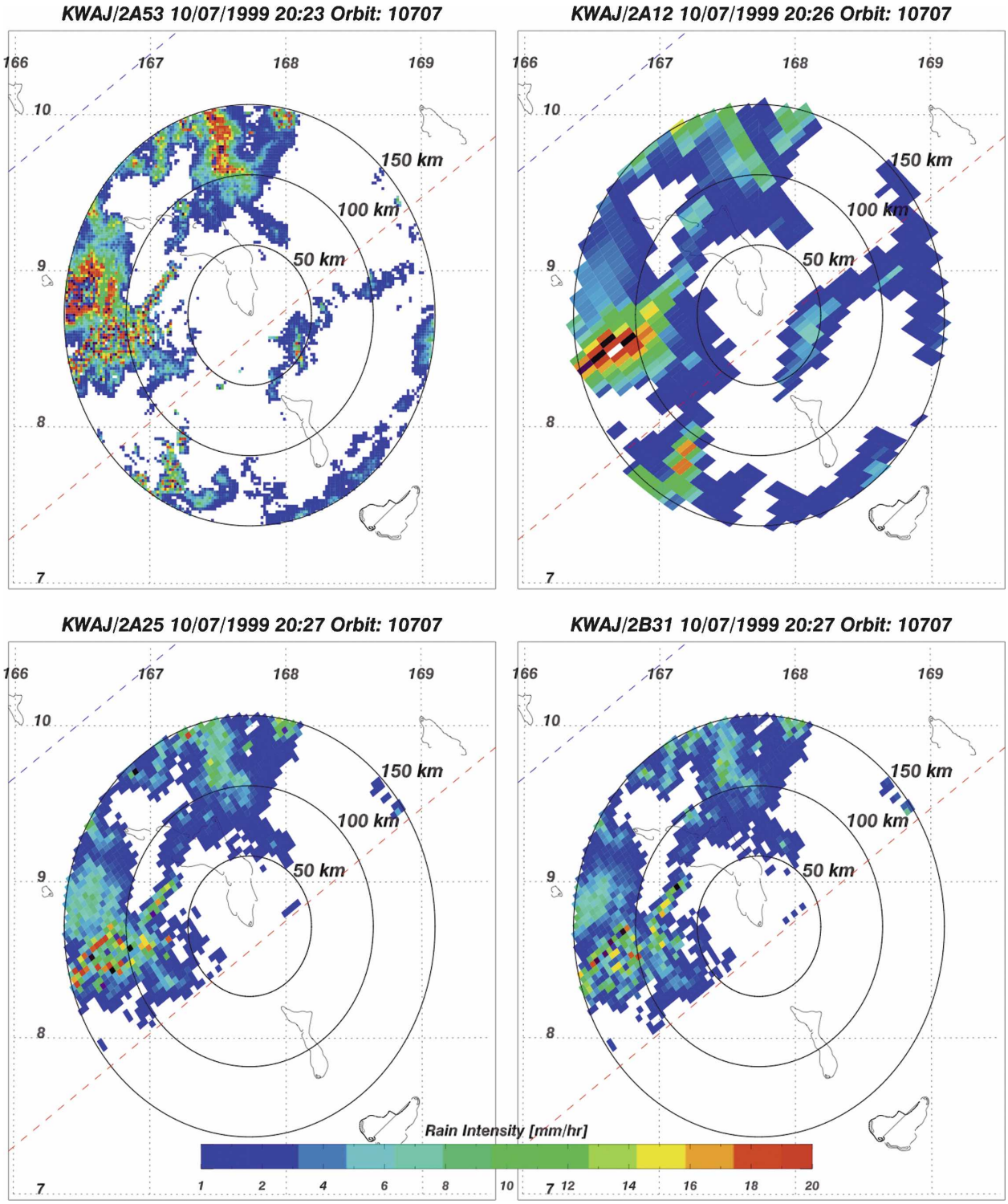

FIG. 9. Illustration of a TRMM overpass of the KWAJ GV sites on 7 Oct 1999 showing the level-II rain data at each instrument's native resolution: (top left) GV 2 km × 2 km, (top right) TMI ~150 km^2 resolution, (bottom left) PR 4 km at nadir, and (bottom right) COM 4 km at nadir.

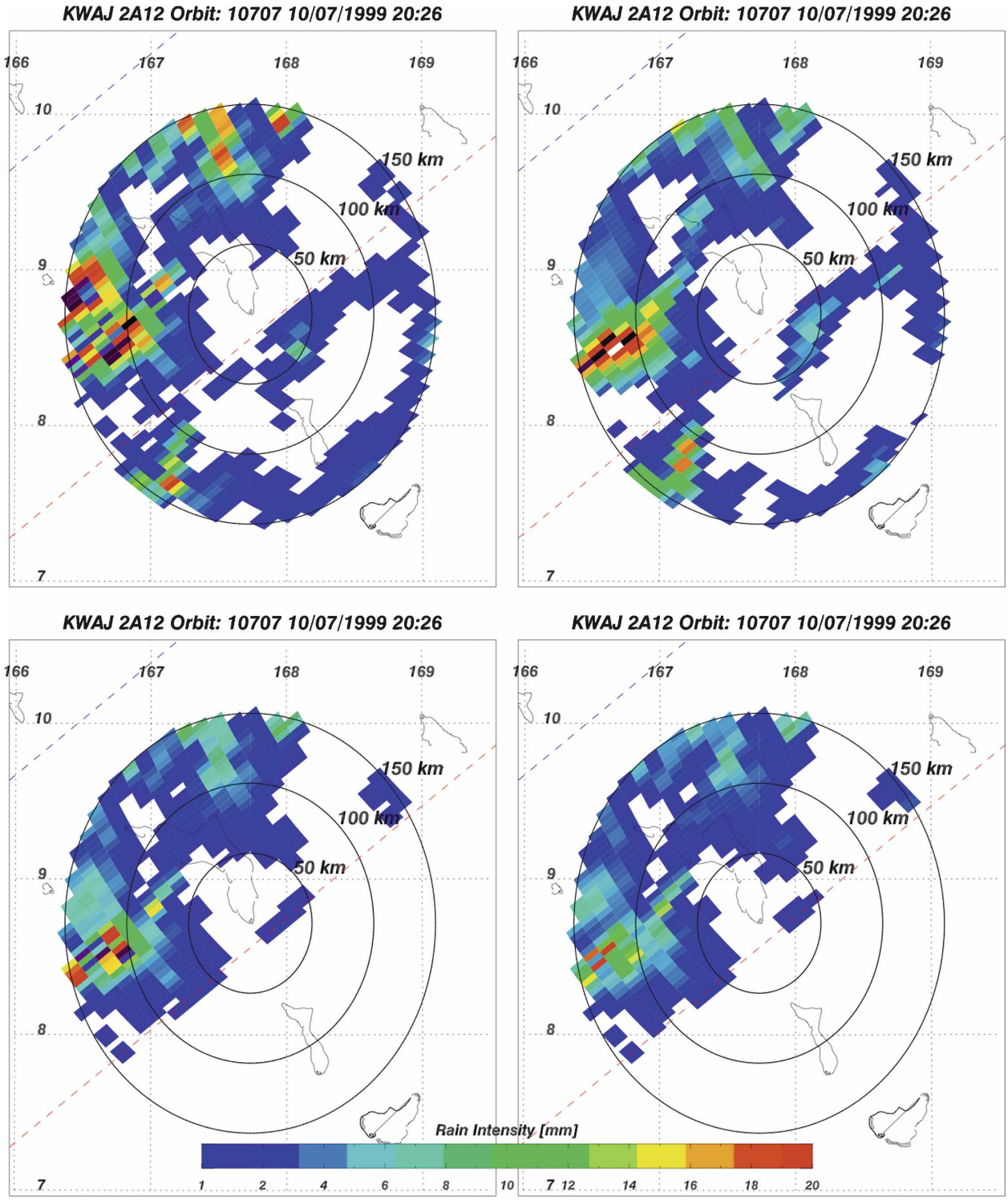

FIG. 10. As in Fig. 9, except that the GV, PR, and COM data have been averaged within each TMI footprint.

values. Even in the low regime, the slopes of each satellite profile reveal systematic differences in the mean rain-rate statistics that provide some explanation for the observed biases in Table 2. Further examination of Figs. 11 and 12 also shows greater variance between the three satellite estimates. It is in the high-rain-rate regimes where the differences between the rainfall algorithms are most apparent. With respect to GV, the

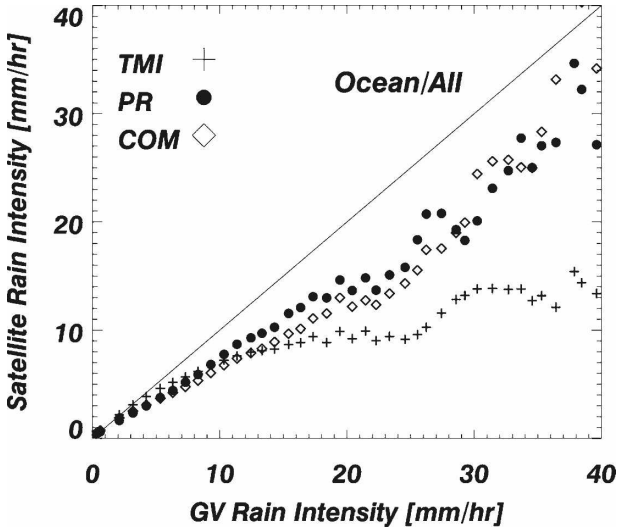

FIG. 11. Comparisons of the TMI, PR, and COM mean rain intensities vs the mean rain intensities of the GV radar at KWAJ. For the case of KWAJ, all TMI pixels are classified as ocean (i.e., ocean/all).

COM rain-rate profile shows the best overall agreement across both the high and low regimes. The PR and COM profiles interestingly appear quite similar in the ocean case for both KWAJ and MELB, but in the land and coast cases, the PR noticeably underestimates the higher rain rates relative to both GV and COM. This behavior dominates the overall profile for MELB shown in Fig. 12 (top left).

The TMI–GV rain-rate profile comparisons reveal the most discrepancies, especially in the high rain-rate regime, and for all terrain categories. Even in the low regime, however, the TMI estimates trends distinctly lower with respect to the GV, PR, and COM estimates. The low slope value observed in the high regime, which is evident in all the panels shown in Figs. 11 and 12, is attributed to the saturation of the TMI signal in the lower channels. The highest TMI rain rates are observed in the land case, which in an examination of Table 2 was the only case where the TMI showed an overall positive bias (+10.2). In every other case, the overall bias was negative. In the MELB land case the determination of the TMI rain rate is empirically determined based on the high-frequency 85-GHz channel and is not dependent on the physical saturation of the signal that naturally occurs in the lower channels.

In the TMI ocean case, mean rain rates rarely exceed 30 mm h^{-1}. The saturation of the lower-frequency TMI channels (10.7, 19.4, 21.3 GHz) was addressed in the original design of the TMI sensor. Based on prior ex-

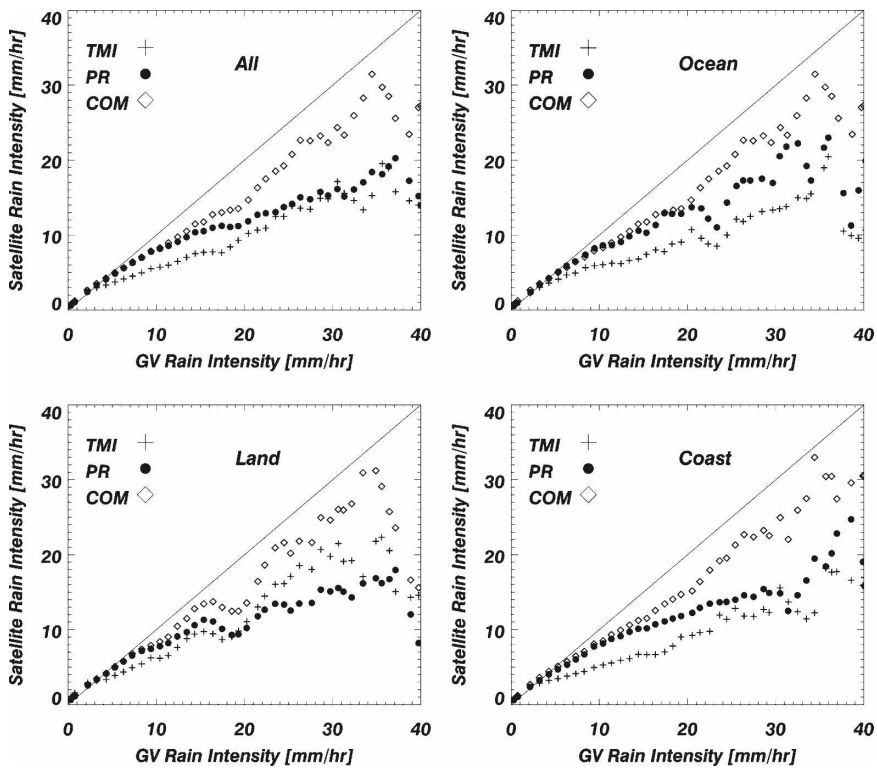

FIG. 12. Comparisons of the TMI, PR, and COM mean rain intensities vs the mean rain intensities of the GV radar at MELB. Rain-rate profiles for (top left) all matched data points; (top right) ocean only, (bottom left) land only, and (bottom right) coast only.

TABLE 4. Melbourne regression parameters (A, all; O, ocean; L, land; C, coast).

Satellite product	TMI surface flag	RR regime (mm h^{-1})	Regression parameters: Intercept (mm h^{-1})	R	Slope
TMI	A	0–20	1.44	0.99	0.40
PR	A	0–20	1.56	0.98	0.60
COM	A	0–20	1.19	1.00	0.68
TMI	O	0–20	2.32	0.98	0.40
PR	O	0–20	1.30	0.99	0.64
COM	O	0–20	1.12	0.99	0.63
TMI	L	0–20	1.53	0.98	0.47
PR	L	0–20	1.97	0.94	0.51
COM	L	0–20	1.35	0.97	0.84
TMI	C	0–20	1.37	0.99	0.58
PR	C	0–20	1.41	0.99	0.58
COM	C	0–20	1.14	1.00	0.70
TMI	A	21–40	6.21	0.69	0.27
PR	A	21–40	7.51	0.73	0.26
COM	A	21–40	4.48	0.86	0.62
TMI	O	21–40	6.93	0.36	0.18
PR	O	21–40	9.08	0.45	0.26
COM	O	21–40	−4.86	0.84	0.91
TMI	L	21–40	13.21	0.27	0.14
PR	L	21–40	12.36	0.11	0.05
COM	L	21–40	16.08	0.25	0.21
TMI	C	21–40	1.75	0.84	0.38
PR	C	21–40	2.97	0.78	0.43
COM	C	21–40	0.44	0.94	0.79

perience with SSMI/I, the water vapor channel was shifted from 22.235 to 21.3 GHz to avoid saturating the signal, in which higher brightness temperatures in the 21.3-GHz channel are correlated with higher rain rates (Kummerow et al. 1998), but this sensor modification obviously did not eliminate the problem entirely and TMI ocean rain rates at both KWAJ and MELB revealed negative biases of −8.8% and −9.2%, respectively. Ha and North (1999), moreover, point out that above 20 mm h^{-1} the scattering of microwave radiation becomes important and causes the relationship between rain rate and brightness temperature to become double valued.

TABLE 5. KWAJ regression parameters (all pixels are classified as ocean).

Satellite product	TMI surface flag	RR regime (mm h^{-1})	Regression parameters: Intercept (mm h^{-1})	R	Slope
TMI	O/A	0–20	1.65	0.97	0.46
PR	O/A	0–20	0.0	1.00	0.74
COM	O/A	0–20	0.39	1.00	0.61
TMI	O/A	21–40	4.37	0.78	0.25
PR	O/A	21–40	−4.50	0.91	0.87
COM	O/A	21–40	−17.12	0.92	1.32

High rainfall gradients also pose a problem for the TMI rain algorithm due to the physical assumption of homogeneity across the rain area associated with the sensor's effective field of view (Wilheit et al. 1991; Kummerow 1998; Kummerow et al. 2001). Kummerow (1998) has noted that in many physical models, this assumption is the largest component of the uncertainty in inferred brightness temperature and leads to a systematic underestimate in the rain rate due to the nonlinear relationship between rain rate and brightness temperature. Beam-filling errors, not surprisingly, are most significant in cases where large brightness temperature gradients exist—those found in association with smaller-scale convection. Small-scale convective systems are quite common across the Florida Peninsula and account for a significant portion of the annual rainfall. In the latest version of GPROF (i.e., version 6), the beam-filling problem for the TMI has been treated in such a way that the uncertainty no longer depends on the computation of a convective–stratiform ratio and instead varies as a constant factor (Kummerow et al. 2001).

The PR rain-rate profile displays more consistency than the TMI profile between the low and high rain-rate regimes, but like the TMI, it also shows signs of saturating at the higher rain rates over land. The v6 PR appears in better agreement for the ocean case shown in Figs. 11 and 12 (top right). With its 4 km^2 resolution, the PR is better able to resolve the small-scale structural features associated with convective rain systems, and because it relates rain-rate observations to the relative amount of power backscattered from the resolution volume, in principle, higher rain rates should be observable. In the three stratified cases for MELB, PR coast shows the best agreement at the high rain rates and the smoothest transition between the low and high parts of the rain-rate spectrum. Note that although the PR algorithm does not depend on the TMI surface flag, it does depend on its own determination of stratiform and convective rain areas, which affects the DSD profile used to convert reflectivities to rain rate.

A comparison of the v5 and v6 PR rain rates with GV over the radar domain at MELB by Amitai et al. (2006) showed significant changes in the PDF of rain rate. Their results indicated that the v5 PR data were in better agreement with GV than that of v6, and tended to underestimate the higher rain rates. They further showed that v6 changes resulted in a reduction of 26% of the convective rainfall and a 13% increase in the amount of stratiform rain. These changes had the effect

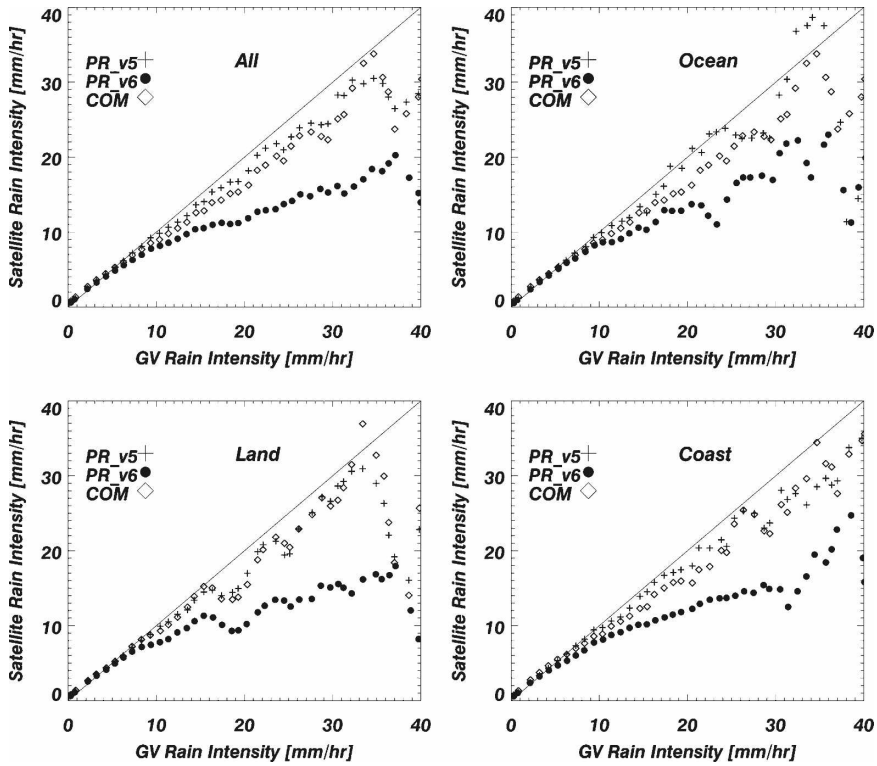

FIG. 13. Comparisons of the PR (v5), PR (v6), and COM rain intensities vs the mean GV rain intensities.

of narrowing the v6 PDFs of the rain rate. Other groups have found similar issues with the v6 rain estimates, especially in convection over land areas, and investigations are currently under way to mitigate the problems.

Figure 13 compares rain-rate profiles for 150 overpasses, also used by Liao et al. (2001), using both v5 and v6 PR data. The version 6 of COM was included to provide a further basis for comparison. The v5 PR rain-rate profile shown in Fig. 13 is in much better agreement with the COM and GV in the high rain-rate part of the spectrum.

The COM–GV regressions in general exhibit less decorrelation at higher rain rates for KWAJ and MELB, and the rain rates at both the high and low regimes tend to increase monotonically with respect to the matching GV rain rates. The slopes in Tables 4 and 5 also show a tendency to increase in the high regime relative to the low regime, in contrast with the TMI and PR, which both exhibited sharp decreases. Although COM shows some consistency with the PR at KWAJ, it deviates from the PR and the TMI in the high rain-rate regime at MELB, especially in the land and coast stratifications. These results for COM are encouraging, but it should also be noted that in Table 2 the COM biases at MELB were consistently positive and absolute values exceeded those of both the TMI and PR. However, Figs. 11 and 12 both suggest that significant improvements in rain estimation can be realized using information from both sensors, even when the individual sensors exhibit different rain characteristics.

c. *Footprint statistics: Standard errors*

The satellite errors were characterized by estimating the error variance between the satellite sensor and the GV rain rate for each binning interval between 0 and 30 mm h^{-1}. The error variance $\sigma^2_{\mathrm{err}}(i)$ was computed at each 1 mm h^{-1} interval by considering all of the matching satellite–GV rain rates within ± 3 mm h^{-1} of the target bin, using the following expression:

$$\sigma^2_{\mathrm{err}}(i) = \mathrm{var}(s_{i\pm 3} - r_{i\pm 3}) = \sigma^2_s(i) + \sigma^2_r(i) - 2\,\mathrm{cov}(s_{i\pm 3}, r_{i\pm 3}), \quad (3)$$

where $s_{i\pm 3}$ and $r_{i\pm 3}$ represent the matching satellite and GV pairs within a ± 3 mm h^{-1} interval centered on the target 1 mm h^{-1} bin, i.

The standard error was then computed by taking the square root of the resulting error variance:

$$\sigma_{\mathrm{err}}(i) = \sqrt{\mathrm{var}(s_{i\pm 3} - r_{i\pm 3})}. \quad (4)$$

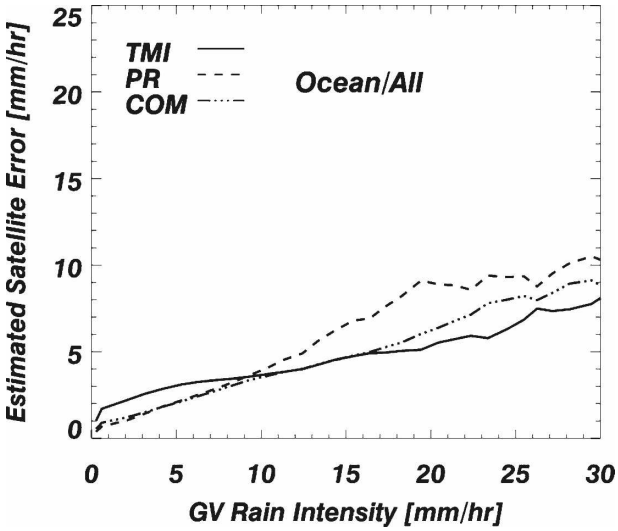

FIG. 14. Profile of the standard errors for TMI, PR, and COM at KWAJ vs the GV rain-rate intensity. Errors were determined based on the variance differences between the matched satellite rain rates and the GV radar at KWAJ. For the case of KWAJ, all TMI pixels are classified as ocean (i.e., ocean/all).

This statistical methodology oversamples the adjacent bins in the neighborhood of i, but has the advantage of increasing the sample sizes of rain rates at the higher bins where the sampling was insufficient ($n < 10$). This strategy was used in lieu of applying a 7 mm h^{-1} mean filter in order to ensure that each variance was based on a sufficiently large sample size (both methods were applied and produced consistent results). The satellite variance $\sigma_s^2(i)$ contributes the most to the error as expressed in (3), while the other two terms nearly cancel out when taken together.

The standard error profiles for KWAJ and MELB are displayed in Figs. 14 and 15, respectively. Like in the previous subsection, the MELB profiles shown in Fig. 15 have been further subcategorized into ocean, land, and coast. The standard errors, as expected, tend to increase monotonically from near 0 at the low end to as high as 15 mm h^{-1} at the high end, showing the relative dependence of the error on rain rate. TMI standard errors over ocean trended significantly lower than those of PR and COM for KWAJ and MELB, and both cases remain in a narrow range confined between 0 and 8 mm h^{-1}. The COM errors in the MELB ocean case show a sharp increase above 23 mm h^{-1}, which is not

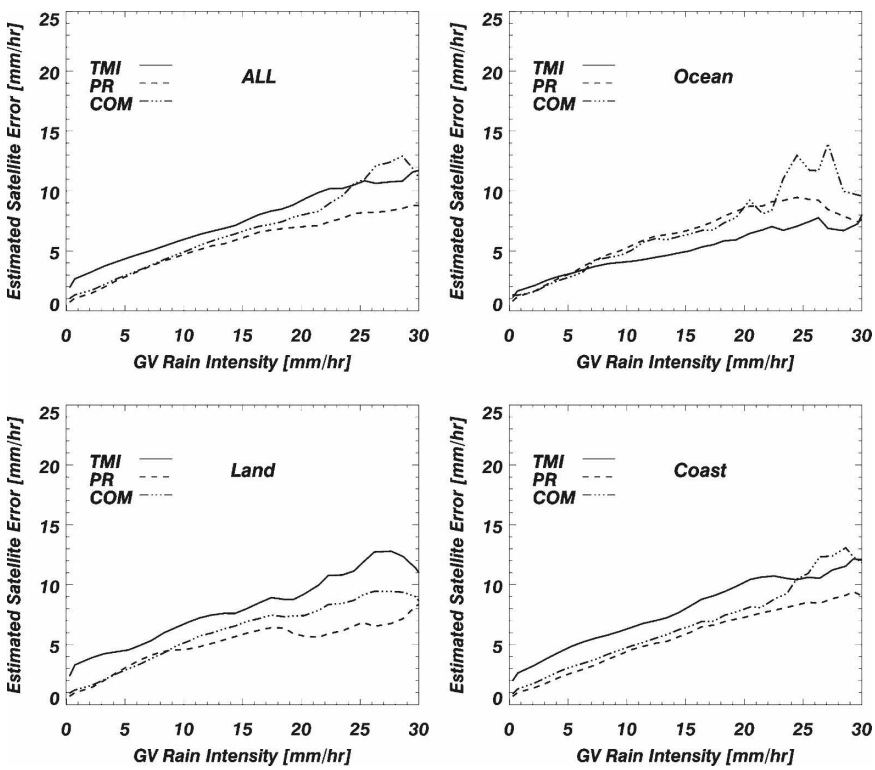

FIG. 15. Profile of the standard errors for TMI, PR and COM at MELB vs the GV rain-rate intensity: (top left) all matched data points, (top right) ocean only, (bottom left) land only, and (bottom right) coast only.

observed at KWAJ; it exhibited similar but less pronounced error characteristics for MELB coast.

The sampling in each case seems to be sufficient, since each 1 mm h^{-1} bin included all of the sampling within a ± 3 mm h^{-1} range. Most sample sizes in the higher bins exceeded 50 for each terrain case; the minimum sample size was 23. The significantly higher variances observed at the higher rain rates in the case of COM should be evaluated in conjunction with the mean statistics shown in Fig. 12. The MELB land profile shown in Fig. 15 (bottom left) exhibits different error characteristics for the TMI and the PR. In this case, the PR trends significantly lower, whereas the TMI tracks more closely with the COM. The COM land case shows monotonically increasing errors, but does not exhibit the sharp increase above 25 mm h^{-1} observed in the ocean and coast cases.

The empirical results shown here inferred from comparisons with GV are consistent with the results from Olson et al. (2006). They applied an algorithm-based method that computed standard errors at the footprint scale (ocean only) using the data from seven complete TRMM orbits. Their results show TMI errors increasing monotonically from 0 to about 15 mm h^{-1} across a range extending between 0 and 30 mm h^{-1}. The results displayed in Figs. 14 and 15 are consistent with those of Olson et al., but these results were derived from regional data, which may exhibit some additional dependence on the regional climatology. The TMI ocean profiles for MELB and KWAJ, for example, are quite similar, especially in the lower range of rain rates below 20 mm h^{-1}. The COM oceanic error characteristics, on the other hand, are significantly different above 20 mm h^{-1}, with errors increasing more sharply in the MELB case. More analysis will be required to verify these inferred error characteristics.

d. Probability distributions at the TMI footprint scale

1) KWAJ

Figure 16 provides the rain-rate PDFs and CDFs for each estimate at the footprint level at KWAJ. Also, shown are the resultant mean rain rates (2.01, 1.59, 1.83, and 1.61 for GV, PR, TMI, and COM, respectively), as well as the total number of "footprints" that were used for averaging the various estimates. Given the large number of points available for generating these distributions, much can be deemed by analysis of the individual PDFs. Most notably, note that the basic shapes of the GV, PR, and COM distributions are quite similar, with rather flat unimodal peaks near 0.5 mm h^{-1}; however, the TMI distribution is much more peaked with a pronounced mode at about 2 mm h^{-1}.

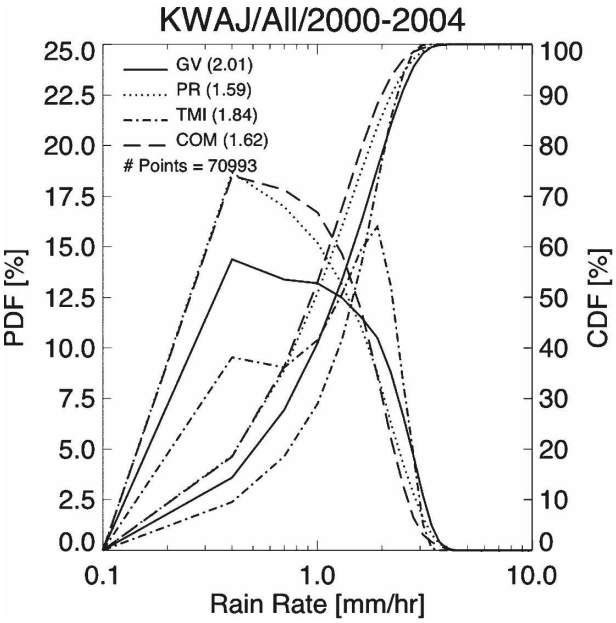

FIG. 16. Plot of the PDFs (curves with peaks) and CDFs of rain rates for GV, PR, COM , and TMI estimates, at the TMI-footprint scale, for the period 1999–2004 at KWAJ.

Overall, the COM and PR CDFs agree the best, and the TMI estimates are considerably higher at all rain rates up to about the 90th percentile (just over 2 mm h^{-1}). Again, as in section 3, we see that the GV CDF falls within the bounds of the other CDFs. An interesting question arises here as to why the TMI PDF is so dissimilar to the other PDFs. Namely, is this due to land effects of the atoll on the TMI estimates (which the algorithm assumes do not exist), or is this an inherent issue with TMI PDFs over ocean? Others have shown some unusual characteristics of TMI oceanic PDFs. In a global study, Yuter et al. (2006) found regional anomalies in the TMI PDFs of rain rate, some of which could be described as "physically implausible."

To determine whether the land areas of the atoll affected the TMI estimates, we subdivided the KWAJ GV domain as illustrated in Fig. 17. In this figure, the shaded regions directly over KWAJ were designated as coast with the remainder of the areas (white region within 150 km from the radar) designated as ocean. As mentioned previously, this rather crude mask, which was used in all TMI products prior to version 6, was at 0.25° resolution. Any 0.25° pixel that contained landmass was assumed to be either coast or land (depending on the amount of land in the given pixel), and using this classification resulted in KWAJ being considered approximately 40% coast (for version-5 algorithmic pur-

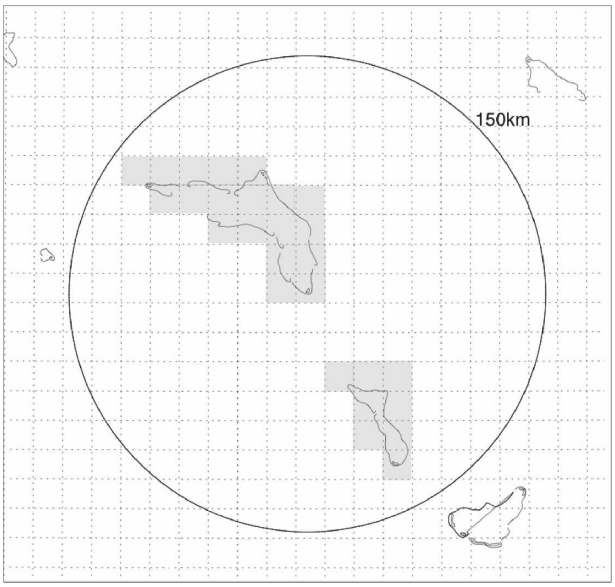

FIG. 17. Subsetted classification of KWAJ using a rough estimate of the TMI v5 surface mask, which considered the areas near the atolls to be coastal.

poses). Note that the data used for this comparison were still from the version-6 database, but the terrain classification was via version-5 surface masking. Figure 18 shows the PDFs of KWAJ rain rates for the various estimates: all, ocean (v5-deemed ocean pixels), and coast (v5-deemed coastal pixels) in the left, middle, and right panels, respectively. While the resultant means are slightly different, the distributions themselves are nearly indistinguishable, which seemingly negates the hypothesis that land effects caused the different behavior of the TMI PDF versus the PDFs of the other estimates.

To investigate whether or not this is possibly due to an inherent issue in ocean TMI estimates, a dataset of distributions of TMI rain rates over 2.5° pixels throughout the tropics compiled by T. Bell (NASA/GSFC, 2006, personal communication) was utilized. It is important to note that the Bell dataset consists of histograms of TMI-footprint rain estimates within each 2.5° grid box, and not histograms of 2.5° gridded rain estimates. Thus, the following comparisons are at the same scale as the Bell dataset. Figure 19 shows an ensemble of monthly PDFs of TMI rain rates for the period 1999–2004, for ocean, land, and coast, in the left, middle, and right panels, respectively. The ocean PDFs clearly show a preferred mode of about 2 mm h^{-1}, as seen over KWAJ and MELB, indicating that there is indeed some algorithmic preference for such estimated rain rates. The land PDF shows the difficulty of estimating light rain rates, given the restrictions imposed by the sole use of ice scattering as a precipitation estimate. Also, the TMI-observable rain rates are significantly higher over land than over ocean. This fact is due to both actual differences in precipitation characteristics over land and ocean, and the failure of the current TMI to estimate higher rain rates over ocean due to the saturation of the signal and beam-filling issues discussed previously.

2) MELB

Figure 20 provides the rain-rate PDFs and CDFs from the various estimates at MELB for all, ocean, land, and coast, in the top-left, top-right, lower-left, and lower-right panels, respectively. What immediately stands out in the "all" PDF is the peaked TMI distribution of rates, with a mode at about 0.8 mm h^{-1}, which differs significantly from all of the other PDFs. A quick examination of the coast PDF shows the dominant effect that coastal areas have on estimated rain rates for the TMI. However, over ocean and land, all of the estimates agree quite well, but there is indeed a noticeable 2 mm h^{-1} TMI rain-rate mode evident at MELB

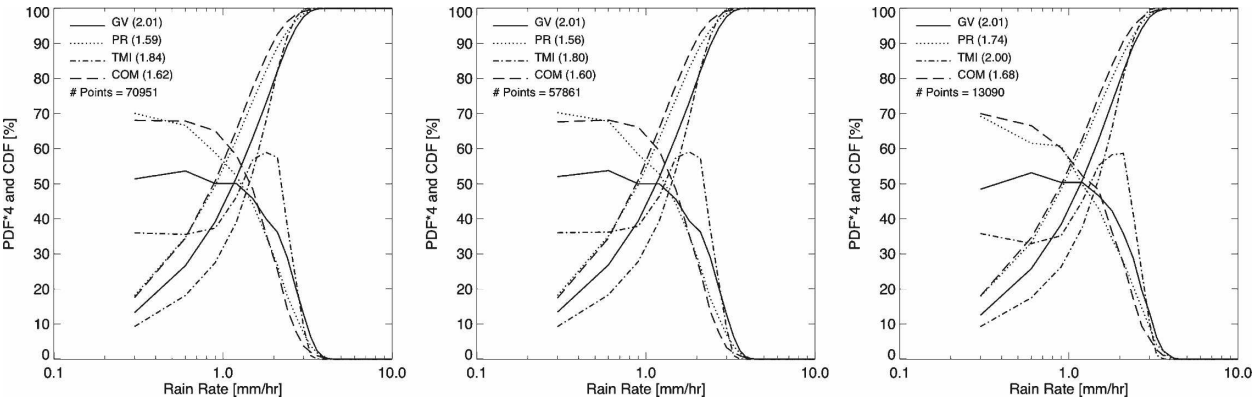

FIG. 18. PDF (curves with peaks) and CDF rain rates at KWAJ over (top left) gray area shown in Fig. 17, (middle) white area in Fig. 17, and all areas (as in Fig. 16).

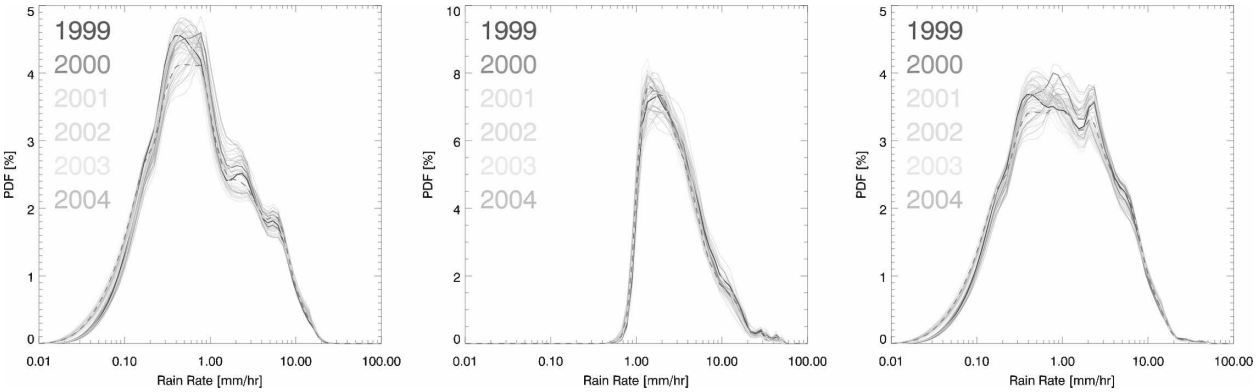

FIG. 19. PDF of TMI rain rates over 2.5° × 2.5° boxes over (top left) ocean, (middle) land, and (right) coast. Curves are shaded by month and year. The boldfaced solid line represents the ensemble of all distributions. The dashed red lines represent August 2001, which corresponds to the period during the TRMM boost from 350 to 402 km. [Data displayed in figure were obtained from Dr. T. Bell (NASA/GSFC).]

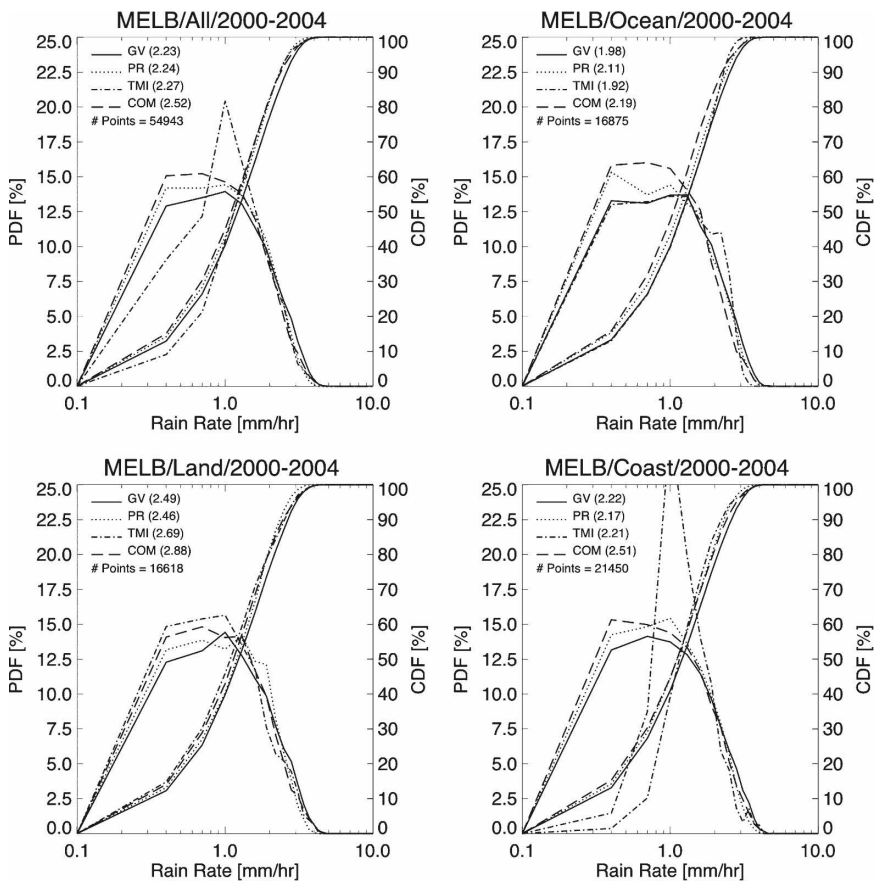

FIG. 20. PDFs (curves with peaks) and CDFs of rain rates at MELB at the TMI-footprint scale for the period 1999–2004 showing GV, PR , COM , and TMI . (top left) The full GV area, (top right) ocean areas only, (bottom left) land areas only, and (bottom right) coastal areas only.

over ocean areas, as was also shown to exist at KWAJ and the tropical oceans in general. The erroneous mode is most probably due to the Bayesian algorithm, and this behavior has been reported to algorithm developers (W. S. Olson et al. 2007, personal communication).

5. Summary and conclusions

TRMM satellite and GV rain rates were spatiotemporally matched and intercompared over two different regional GV sites for the period 1999–2004. These intercomparisons were performed at two different scales: at $0.5° \times 0.5°$ (corresponding to the resolution of the TRMM 3G68 product) and at the nominal scale of the TMI footprint (approximately 150 km^2). It was shown that all of the estimates agree well, but there were some notable differences, especially during heavy rain events and peak rainfall periods. These differences were attributed to the spatiotemporal characteristics of the various rain sensors in conjunction with the observed precipitation events, differences in the way active and passive remote sensing interpret and process rain information, and systematic variations in the physical applications of the different rain algorithms.

Some of the discrepancies were shown to be dependent on the geographical terrain over which the various estimates were made. Over land, for example, the TMI algorithm cannot resolve light rain rates ($<\sim 0.8$ mm h^{-1}) because the algorithm only uses the 85-GHz scattering signal and this precipitation tends not to be as highly correlated with ice processes aloft. The TMI coastal algorithm was also shown to have problems due to the partitioning of these regions into land and ocean sectors. This poses an intrinsic problem for GV, as was shown in Table 1. The GV sites consist of a much higher fraction of coastal pixels relative to the complete sampling domain of the TRMM satellite. In the case of the PR, on the other hand, attenuation of the high-frequency radar signal limits the ability of the PR to resolve areas of deep convection over land and to some extent over ocean. Over ocean, the TMI is better able to resolve the lighter rain rates (~ 0.02 mm h^{-1}), but the precipitation signal in the lower channels becomes saturated at higher rain rates (~ 20 mm h^{-1}).

While analysis of the probability distributions was difficult for the 3G68 comparisons, due to the limited sample size, a much more robust number of observations was available at the TMI footprint scale (approximately 12 000 and 9200 samples per year for KWAJ and MELB, respectively). Our analysis showed that the PDFs of the GV, PR, and COM were quite similar to one another. The TMI PDFs compared to the other three revealed significant structural differences. One of the key findings of this work is the pronounced effect that coastal areas have on the retrieved distribution of rain rates, especially by the TMI. Although it is well known that there are problems for passive microwave estimation of rain intensities over coastal areas, it was shown that the full-GV-area probability distributions of rain rates are strongly influenced by coastal algorithm uncertainties. It then stands to reason that validating TRMM estimates without removing coastal-area estimates will significantly increase the quantitative uncertainty and, at the very least, lead to a misinterpretation of the results.

Satellite–GV intercomparisons at the footprint scale showed reasonably good agreement in the lower half of the rain-rate spectrum, with the most salient differences observed at the higher rain rates. In the comparisons to GV, the v6 TMI and v6 PR appear to be underestimating the higher rain rates. This issue, interestingly, appeared to be somewhat mitigated in similar comparisons performed using v5 data. This same result, as discussed earlier, has been noted in other studies and is currently being investigated by the developers of the PR algorithm. An evaluation of the mean rain-rate spectrum suggested that COM performed better at the higher rain rates relative to GV than either v6 TMI or v6 PR. But in some cases the COM errors were significantly higher, perhaps suggesting an inconsistent handling of the high rain-rate cases. This result will need to be more closely examined in future work. Although more work needs to done, the results from the footprint part of the study are encouraging because they show that statistically meaningful GV–satellite intercomparisons can be performed at the spatiotemporal scale of the TMI footprint, provided there exists a sufficiently large sample of overpasses.

It was also shown that there is a preferred mode in the TMI rain-rate distributions at approximately 2 mm h^{-1} that was not evident in any of the other distributions, thus indicating that more work needs to be done to improve the over-ocean estimates by the TMI algorithm developers.

Acknowledgments. This work was funded by NASA Grant NNG07EJ50C. The authors thank Dr. Ramesh Kakar (NASA Headquarters), Dr. Robert Adler (TRMM project scientist), and Mr. Richard Lawrence (chief, TRMM Satellite Validation Office) for their support of this effort. We also appreciate the support staff of the TSVO, including David Makofski, Bart Kelley, David Marks, David Silberstein, and Jason Pippitt.

REFERENCES

Amitai, E., X. Llort, and D. Sempere-Torres, 2006: Opportunities and challenges for evaluating precipitation estimates during GPM mission. *Meteor. Z.,* **15,** 551–557.

Bell, T. L., and P. K. Kundu, 1996: A study of sampling error of satellite rainfall estimates using averaging of data and a stochastic model. *J. Climate,* **9,** 1251–1268.

——, and ——, 2000: Dependence of satellite sampling error on monthly averaged rain rates: Comparison of simple models and recent studies. *J. Climate,* **13,** 449–462.

——, A. Abdullah, R. L. Martin, and G. North, 1990: Sampling errors for satellite-derived tropical rainfall: Monte Carlo study using a space–time stochastic model. *J. Geophys. Res.,* **95,** 2195–2205.

——, P. K. Kundu, and C. D. Kummerow, 2001: Sampling errors of SSM/I and TRMM rainfall averages: Comparison with error estimates from surface data and a simple model. *J. Appl. Meteor.,* **40,** 938–954.

Conner, M. D., and G. W. Petty, 1998: Validation and intercomparison of SSM/I rain-rate retrieval methods over the continental United States. *J. Appl. Meteor.,* **37,** 679–700.

Ferraro, R. R., 1997: Special Sensor Microwave Imager derived global rainfall estimates for climatological applications. *J. Geophys. Res.,* **102,** 16 715–16 735.

Fisher, B. L., 2004: Climatological validation of TRMM TMI and PR monthly rain products over Oklahoma. *J. Appl. Meteor.,* **43,** 519–535.

——, 2007: Statistical error decomposition of regional-scale climatological precipitation estimates from the Tropical Rainfall Measuring Mission (TRMM). *J. Appl. Meteor. Climatol.,* **46,** 791–813.

Ha, E., and G. R. North, 1999: Error analysis for some ground validation designs for satellite observations of precipitation. *J. Atmos. Oceanic Technol.,* **16,** 1949–1957.

Houze, R. A., S. Brodzik, C. Schumacher, S. E. Yuter, and C. R. Williams, 2004: Uncertainties in oceanic radar rain maps at Kwajalein and implications for satellite validation. *J. Appl. Meteor.,* **43,** 1114–1132.

Iguchi, T., T. Kozu, R. Meneghini, J. Awaka, and K. Okamoto, 2000: Rain-profiling algorithm for the TRMM Precipitation Radar. *J. Appl. Meteor.,* **39,** 2038–2052.

Kummerow, C., 1998: Beamfilling errors in passive microwave rainfall retrievals. *J. Appl. Meteor.,* **37,** 356–369.

——, W. S. Olson, and L. Giglio, 1996: A simplified scheme for obtaining precipitation and vertical hydrometeor profiles from passive microwave sensors. *IEEE Trans. Geosci. Remote Sens.,* **34,** 1213–1232.

——, W. Barnes, T. Kozu, J. Shiue, and J. Simpson, 1998: The Tropical Rainfall Measuring Mission (TRMM) sensor package. *J. Atmos. Oceanic Technol.,* **15,** 809–817.

——, and Coauthors, 2001: The evolution of the Goddard profiling algorithm (GPROF) for rainfall estimation from passive microwave sensors. *J. Appl. Meteor.,* **40,** 1801–1820.

Laughlin, C. R., 1981: On the effect of temporal sampling on the observation of mean rainfall. *Precipitation Measurements from Space,* D. Atlas and O. Thiele, Eds., NASA Publ., D59–D66.

Liao, L., R. Meneghini, and T. Iguchi, 2001: Comparisons of rain rate and reflectivity factor derived from the TRMM precipitation radar and the WSR-88D over the Melbourne, Florida, site. *J. Atmos. Oceanic Technol.,* **18,** 1959–1974.

Marks, D. A., D. B. Wolff, D. S. Silberstein, J. L. Pippitt, and J. Wang, 2005: Improving radar rainfall estimates at Kwajalein Atoll, RMI through relative calibration adjustment. Preprints, *32nd Conf. on Radar Meteorology,* Albuquerque, NM, Amer. Meteor. Soc., 3R.2. [Available online at http://ams.confex.com/ams/pdfpapers/96535.pdf.]

McCollum, J. R., and R. R. Ferraro, 2003: Next generation of NOAA/NESDIS TMI, SSM/I, and AMSR-E microwave land rainfall algorithms. *J. Geophys. Res.,* **108,** 8382, doi:10.1029/2001JD001512.

——, and ——, 2005: Microwave rainfall estimation over coasts. *J. Atmos. Oceanic Technol.,* **22,** 497–512.

Meneghini, R., T. Iguchi, T. Kozu, L. Liao, K. Okamoto, J. A. Jones, and J. Kwiatkowski, 2000: Use of the surface reference technique for path attenuation estimates from the TRMM Precipitation Radar. *J. Appl. Meteor.,* **39,** 2053–2070.

Oki, R., and A. Sumi, 1994: Sampling simulation of TRMM rainfall estimation using radar–AMeDAS composites. *J. Appl. Meteor.,* **33,** 1597–1608.

Olson, W. S., and Coauthors, 2006: Precipitation and latent heating distributions from satellite passive microwave radiometry. Part I: Improved method and uncertainty estimates. *J. Appl. Meteor. Climatol.,* **45,** 702–720.

Shin, K., and G. R. North, 1988: Sampling error study for rainfall estimate by satellite using a stochastic model. *J. Appl. Meteor.,* **27,** 1218–1231.

Silberstein, D. S., D. B. Wolff, D. A. Marks, and J. L. Pippitt, 2008: Ground clutter as a monitor of radar stability at Kwajalein, RMI. *J. Atmos. Oceanic Technol.,* in press.

Simpson, J., R. F. Adler, and G. R. North, 1988: A proposed Tropical Rainfall Measuring Mission (TRMM) satellite. *Bull. Amer. Meteor. Soc.,* **69,** 278–294.

Spencer, R., W. H. Goodman, and R. E. Hood, 1989: Precipitation retrieval over land and ocean with the SSM/I: Identification and characteristics of the scattering signal. *J. Atmos. Oceanic Technol.,* **6,** 254–273.

Steiner, M., T. L. Bell, Y. Zhang, and E. F. Wood, 2003: Comparison of two methods of sampling-related uncertainty of satellite rainfall estimates based on a large radar dataset. *J. Climate,* **16,** 3759–3778.

Stocker, E. F., J. Kwiatkowski, and O. Kelley, 2001: Gridded hourly text products: A TRMM data reduction approach. *Proc. 2001 Int. Geoscience and Remote Sensing Symposium,* Sydney, Australia, IEEE, 658–660.

Tao, W.-K., and J. Simpson, 1993: Goddard Cumulus Ensemble Model. Part I: Model description. *Terr. Atmos. Oceanic Sci.,* **4,** 35–72.

Thiele, O., 1988: Validating space observations of rainfall. *Tropical Rainfall Measurements,* J. S. Theon and N. Fugono, Eds., A. Deepak, 415–423.

Wilheit, T. T., A. Chang, and L. Chiu, 1991: Retrieval of monthly rainfall indices from microwave radiometric measurements using probability distribution function. *J. Atmos. Oceanic Technol.,* **8,** 118–136.

Wilheit, T., C. Kummerow, and R. Ferraro, 2003: Rainfall algorithms for AMSR-E. *IEEE Trans. Geosci. Remote Sens.,* **41,** 204–214.

Wolff, D. B., D. A. Marks, E. Amitai, D. S. Silberstein, B. L. Fisher, A. Tokay, J. Wang, and J. L. Pippitt, 2005: Ground validation for the Tropical Rainfall Measuring Mission (TRMM). *J. Atmos. Oceanic Technol.,* **22,** 365–380.

Yuter, S., M. Miller, J. Stout, R. Wood, J. Kwiatkowski, D. Horn, and C. Spooner, 2006: Remaining challenges in satellite precipitation estimation for the Tropical Rainfall Measuring Mission. Preprints, *Fourth European Conf. on Radar in Meteorology and Hydrology,* Barcelona, Spain, Copernicus Gesellschaft mbH and European Meteorological Society, 18–22. [Available online at http://www4.ncsu.edu/~seyuter/pdfs/ERAD06TRMM00163.pdf.]